Journal of Extracellular Vesicles

SHORT COMMUNICATION OPEN ACCESS

Stress-Induced Switch in Small Extracellular Vesicle Secretion: From Constitutive 'Torn Bag Mechanism' to Exocytosis

Dorina Lenzinger[1] | Lilla Lankovics[1] | István Dudás[1] | Tünde Bárkai[1] | Zsófia Szász[1] | Mirjam Balbisi[2] | Anthony Yan-Tang Wu[3,4] | Krisztina V. Vukman[1] | Kelsey Fletcher[1] | Attila Csomos[5] | Zoltán Mucsi[6] | Edina Bugyik[1] | Csaba Cserép[7] | Ádám Dénes[7] | Szilvia Bősze[1,8] | Lilla Turiák[2] | Charles Pin-Kuang Lai[3,4,9] | Edit I. Buzás[1,10] | Tamás Visnovitz[1,11]

[1]Institute of Genetics, Cell- and Immunobiology, Semmelweis University, Budapest, Hungary | [2]MTA-HUN-REN TTK Lendület (Momentum) Glycan Biomarker Research Group, HUN-REN Research Centre for Natural Sciences, Budapest, Hungary | [3]Institute of Atomic and Molecular Sciences, Academia Sinica, Taipei, Taiwan | [4]Chemical Biology and Molecular Biophysics Program, Taiwan International Graduate Program (TIGP), Academia Sinica, Taipei, Taiwan | [5]Department of Chemistry, Faculty of Natural Sciences, ELTE Eötvös Loránd University, Budapest, Hungary | [6]Faculty of Materials and Chemical Engineering, Institute of Chemistry, University of Miskolc, Miskolc, Hungary | [7]Laboratory of Neuroimmunology, HUN-REN Institute of Experimental Medicine, Budapest, Hungary | [8]HUN-REN-ELTE Research Group of Peptide Chemistry, ELTE Eötvös Loránd University, Budapest, Hungary | [9]Genome and Systems Biology Degree Program, National Taiwan University, Taipei, Taiwan | [10]HUN-REN-SU Translational Extracellular Vesicle Research Group, Budapest, Hungary | [11]Department of Plant Physiology and Molecular Plant Biology, ELTE Eötvös Loránd University, Budapest, Hungary

Correspondence: Edit I. Buzás (buzas.edit@semmelweis.hu) | Tamás Visnovitz (visnovitz.tamas@semmelweis.hu)

Received: 27 October 2025 | **Revised:** 21 May 2026 | **Accepted:** 7 July 2026

Keywords: amphiectosome | autophagy | exocytosis | exosome secretion | stress | 'torn bag mechanism' | small extracellular vesicles

ABSTRACT

The biogenesis of small extracellular vesicles (sEVs) is only partially understood. Our recent findings provide evidence that a newly described sEV secretion pathway, the amphiectosome release followed by the sEV discharge by the 'torn bag mechanism' are present in all tested cell lines and mouse organs. Surprisingly, in in situ fixed steady-state cells, transmission electron microscopy did not reveal sEV release via exocytosis of multivesicular endosomes (MVEs). In the current study, we extended our previous analysis to additional mouse organs and confirmed the presence of secreted amphiectosomes in all of them. Furthermore, we investigated which parameters influence the activation of the distinct sEV release mechanisms in HEK cells. Our results show that under stress conditions (such as Ca^{2+} ionophore-induced membrane stress or metabolic stress, induced by serum starvation), exocytosis of MVEs is activated, while this process is absent in steady-state conditions. By silencing ATG5 (a key regulator of autophagy) and RAB27a (an essential small GTPase for MVE exocytosis), we selectively modulated these two mechanisms, respectively. Amphiectosome release depended on both autophagy and ATG5, while exocytosis of MVE was autophagy-independent but RAB27a-dependent. Our findings suggest that sEV release via the 'torn bag mechanism' is a general and essential secretion pathway in non-stressed, steady-state mammalian cells, while stress conditions induce the sEV release via MVE exocytosis.

Edit I. Buzás and Tamás Visnovitz contributed equally to this work.

1 | Introduction

Extracellular vesicles (EVs) are particles enclosed by a phospholipid bilayer that facilitate intercellular communication (Welsh et al. 2024; Théry et al. 2018), and exosomes are a subset of EVs of endosomal origin (Welsh et al. 2024; Buzas 2023). These small EVs (sEVs), typically less than 200 nm in diameter, are formed by the inward budding of the limiting membrane of late endosomes or multivesicular bodies (MVBs) (Kowal et al. 2014; van Niel et al. 2018). Exosome release is considered to be associated with the exocytosis of intraluminal vesicles (ILVs) of multivesicular endosomes (MVEs) (Kowal et al. 2014; Dixson et al. 2023). In contrast, ectosomes bud directly from the cell surface surrounded by the plasma membrane-derived phospholipid membrane (Welsh et al. 2024; Buzas 2023; Dixson et al. 2023). Recent studies have uncovered an unexpected complexity in EV biogenesis (Buzas 2023). We recently reported that the endosomal and plasma membrane origins of EVs are not necessarily mutually exclusive (Valcz et al. 2019; Visnovitz et al. 2025). In colorectal carcinoma cells, we described the ectocytotic release of 'MVB-like sEV clusters' containing ILVs of endosomal origin (Valcz et al. 2019).

Our latest findings also provided evidence for a novel, active, autophagy-dependent, exocytosis-independent sEV secretion pathway, termed amphiectosome release and 'torn bag mechanism' (Visnovitz et al. 2025). Interestingly, both the ILVs of amphiectosomes and the sEVs separated from conditioned media were exclusively positive either for the classical sEV markers (such as CD63, CD81, ALIX and TSG101) or LC3B, suggesting either MVB or autophagy origin of these vesicles. According to our proposed model, upon fusion of MVBs with autophagosomes, fragments of the autophagosomal inner membrane curl up to form LC3B-positive ILVs within amphisomes. In contrast, the CD63-positive sEVs are of presumed MVB origin. The amphisomes are shed from the plasma membrane via ectocytosis as amphiectosomes, which subsequently release their ILVs into the extracellular space through the 'torn bag mechanism' (Visnovitz et al. 2025). The amphiectosome release and 'torn bag' sEV secretion mechanism appear to be frequent biological processes, as we identified them in all tested cell cultures as well as in mouse kidney and liver tissues (Visnovitz et al. 2025). Although the classical exosome release mechanism is linked to the exocytosis of MVBs (Kowal et al. 2014; Dixson et al. 2023) or amphisomes (Dixson et al. 2023; Jeppesen et al. 2019), there is relatively limited ultrastructural evidence supporting this process (Harding et al. 1983; Pan et al. 1985; Raposo and Stoorvogel 2013; Relucenti et al. 2022; De Paoli et al. 2018). Most of these studies have been conducted on special cell types such as reticulocytes (Harding et al. 1983; Pan et al. 1985), immune cells (Raposo and Stoorvogel 2013), platelets (De Paoli et al. 2018) or tumour cells (Relucenti et al. 2022).

In contrast to the data in the literature, we have not detected obvious MVE exocytosis in cell cultures or in ultrathin sections of various mammalian tissues under steady state conditions. Recent findings suggest that Ca^{2+} influx can trigger MVB exocytosis and exosome release, potentially playing a role in plasma membrane repair through the ANX6 protein (Williams et al. 2023). Here we investigated the 'torn bag mechanism' and MVE exocytosis in sEV secretion using HEK cells as it was reported previously (Williams et al. 2023). Specifically, we examined how metabolic or Ca^{2+} ionophore stress influence the activation of these two sEV secretion pathways and found that exocytosis is induced by cellular stress.

2 | Materials and Methods

2.1 | Cell Lines

The HEK293 human embryonic kidney cell line (#85120602, Batch No: 18E026) was purchased from the European Collection of Authenticated Cell Cultures (ECACC) through their distributor (Sigma), the HEK293T-PalmGFP human embryonic kidney cells were kindly provided by Charles P. Lai (Lai et al. 2015). The HEK293T-PalmGFP-LC3RFP cell line was developed by our research group previously (Visnovitz et al. 2025). All HEK293 cell lines were grown in DMEM (Gibco) with 10% foetal bovine serum (FBS, BioSera) in the presence of 2 µmol/mL l-glutamine (Sigma), 100 U/mL of Penicillin and 100 µg/mL Streptomycin (Sigma) (Németh et al. 2021). Before microscopy sample preparation, the cells were cultured on the surface of 0.02% gelatin (Sigma) and 5 µg/mL fibronectin (Invitrogen) coated glass coverslips (VWR) (Koncz et al. 2023). For live cell imaging, cells were cultured on gelatin-fibronectin coated CELLview culture slides (Greiner Bio-One). In order to minimise the genetic drift, master cell banks (MCBs) and subsequently, working cell banks (WCBs) were established. Vials of the characterised WCBs were used for experiments. The cell banks were tested for Mycoplasma infection by PCR (Koncz et al. 2023).

2.2 | Generation of HEK293T-PalmSORET-CD63GFP-LC3RFP Stable Cell Line

Molecular cloning of PalmSORET plasmid: The palmitoylation signal sequence (Wu et al. 2020) was molecularly fused to the 5′ end of iRFP713-Rluc8.6-535SG (Nishihara et al. 2019). The iRFP713 fragment was cloned from pcDNA3.1_iSH2-pMag(3×)-iRFP (a gift from Moritoshi Sato; Addgene plasmid #67304) (Kawano et al. 2015). Rluc8.6-535SG was generated by site-directed mutagenesis of Rluc8 from Nano-lantern/pcDNA3 (a gift from Takeharu Nagai; Addgene plasmid #51970) (Saito et al. 2012). The iRFP713 and Rluc8.6-535SG fragments were cloned into a pENTR backbone generated by digesting pENTR-Luc (w158-1; a gift from Drs. Eric Campeau and Paul Kaufman; Addgene plasmid #17473) (Campeau et al. 2009) with NcoI and XbaI (New England Biolabs), followed by assembly using NEBuilder HiFi DNA Assembly (New England Biolabs) to generate pENTR-PalmSORET. The pLenti DEST CMV Puro-PalmSORET plasmid was generated by Gateway LR recombination between pENTR-PalmSORET and pLenti DEST CMV Puro (a gift from Drs. Eric Campeau and Paul Kaufman; Addgene plasmid #17452) (Campeau et al. 2009) using LR Clonase II Plus (Invitrogen, Carlsbad, CA, USA).

Lentiviral Production: PalmSORET (Palm-iRFP713-Rluc8.6-535SG) lentiviral particles were produced according to the

Addgene lentivirus production protocol (https://www.addgene.org/protocols/lentivirus-production/) with minor modifications. Briefly, HEK293T cells were seeded in 10 cm dishes and cultured to 70%–80% confluence. Five hours prior to transfection, the medium was replaced with 10 mL of DMEM supplemented with GlutaMAX (Gibco), 10% heat-inactivated FBS (HyClone) and 25 μM chloroquine diphosphate (Tokyo Chemical Industry). Cells were co-transfected with 1.3 pmol psPAX2 (a gift from Dr. Didier Trono; Addgene plasmid #12260), 0.72 pmol pMD2.G (a gift from Dr. Didier Trono; Addgene plasmid #12259) and 1.64 pmol pLenti DEST CMV Puro-PalmSORET using linear polyethylenimine (PEI; MW 25 000; 1 mg/mL; Alfa Aesar) at a DNA-to-PEI ratio of 1:3. Transfection complexes were prepared in 1 mL of Opti-MEM (Gibco). At 18 h post-transfection, the medium was replaced with 15 mL of virus production medium (DMEM supplemented with GlutaMAX and 10% heat-inactivated FBS). Viral supernatants were collected at 48 h post-transfection, stored at 4°C, and replaced with 15 mL of fresh virus production medium. A second collection was performed at 72 h post-transfection. The pooled supernatants were clarified by centrifugation at 500 *g* for 10 min at 4°C, filtered through a 0.45 μm PES membrane (Pall), aliquoted into 1 mL cryovials, snap-frozen in liquid nitrogen and stored at –80°C until use.

Generation of Stable HEK293T-PalmSORET Cell Lines: Stable HEK293T-PalmSORET cell lines were established following a modified Addgene protocol for generating stable cell lines (https://www.addgene.org/protocols/generating-stable-cell-lines/). Briefly, graded volumes (0.5, 1 and 2 mL) of PalmSORET lentiviral supernatant were added to wells of a 6-well plate. A suspension of HEK293T cells prepared in high-glucose DMEM (HyClone) supplemented with 10% heat-inactivated FBS (HyClone), 10 μg/mL polybrene (Sigma–Aldrich) and 1× GlutaMAX (Gibco) was then added dropwise to each well. Following medium replacement and cell expansion, transduced cell populations were enriched for iRFP713-positive (R712) cells using a CytoFLEX SRT fluorescence-activated cell sorter (Beckman Coulter). Stable cells were maintained in high-glucose DMEM (4500 mg/L; HyClone) supplemented with 10% FBS (HyClone) and penicillin-streptomycin (100 U/mL and 100 μg/mL, respectively; HyClone). Early-passage cells were frozen and stored after sorting.

Generation of Multi-Fluorescent Stable Cell Line: Stable HEK293T-PalmSORET cells were cultured in 35 mm glass-bottom Petri dishes (VWR) containing 1 mL of culture medium. After 24 h 10 μL of CD63-GFP lentiviral particles (RC201733L4V, OriGene) were added. Cells were subsequently maintained and expanded. Stable iRFP713 and GFP double-positive cells were sorted using a SONY SH800 flow cytometer (Sony). Following validation, HEK293T-PalmSORET-CD63GFP stable cells were over transfected with 5 μL of LC3-RFP lentiviral particles (17-10143, Merck), as described previously (Visnovitz et al. 2025). Triple-positive (GFP, RFP and iRFP713) HEK293T-PalmSORET-CD63GFP-LC3RFP cells were sorted using a SONY SH800 flow cytometer. The resulting cell line was validated (Figure S4) and properly banked: a master cell bank (P2) and a working cell bank (P6) were established. All experiments were initiated from cryovials derived from the working cell bank. The cell banks were tested for Mycoplasma infection by PCR (Koncz et al. 2023).

2.3 | Mice

C57BL/6 mice were purchased from The Jackson Laboratory and bred in a pathogen-free animal facility at the Institute of Genetics, Cell and Immunobiology, Semmelweis University. For transmission electron microscopy, 12-week-old male mice were used and sacrificed in accordance with the Animal Experimentation Code of Semmelweis University.

2.4 | Transmission Electron Microscopy

Tissue samples from mouse organs (approximately 1 mm^3) were immersed and fixed in 4% glutaraldehyde (Sigma) for at least 24 h at 4°C, followed by post-fixation in 1% osmium tetroxide (SPI) for 2 h at room temperature (RT). For embedding, an EPON resin mixture (SPI) was applied as described previously (Visnovitz et al. 2025, Olah et al. 1992). Sample preparation of HEK293 cells was performed on the surface of glass coverslips placed in a 24-well untreated cell culture plate (Eppendorf). For monolayer cell cultures, propylene oxide (typically used as a solvent for EPON resin) was omitted and replaced with absolute ethanol. After polymerisation of the resin (at least 48 h at 56°C), the glass coverslips were removed using liquid nitrogen. For analysis of the secreted extracellular particles under Ca^{2+} ionophore-induced stress, serum- and cell-free conditioned media were concentrated using TFF Easy (Hansa Biomed) and subsequently pelleted by ultracentrifugation at 100 000 *g for 70 min* using an MLA-55 rotor in an Optima MAX-XP benchtop ultracentrifuge (Beckman Coulter) at 4°C. The pellets were fixed in 4% glutaraldehyde for 24 h at 4°C, followed by post-fixation with 1% osmium tetroxide for 2 h at RT. Samples were then embedded in an EPON resin mixture. Ultrathin sections (50–70 nm) were made using an RMC Boeckeler PowerTome ultramicrotome. Sections were post-contrasted with UranyLess (Electron Microscopy Sciences) for 10 min at RT, followed by 2 min in lead citrate (RT) (Reynolds 1963). Images were captured using a JEM-1010 transmission electron microscope (JEOL) equipped with a 3-megapixel Veleta digital camera with the help of Olympus iTEM software (version 5.1).

2.5 | Immunofluorescent Microscopies

Confocal microscopy was performed as previously described (Visnovitz et al. 2025). Cells were cultured on a gelatin/fibronectin-coated surface. To study the cellular microenvironment around the cultured cells, the cultures were not washed before fixation; both cells and their microenvironment were fixed 'in situ'. Without changing the culture medium, 8% paraformaldehyde (PFA) in PBS was added in an equal volume to achieve a final concentration of 4%. After fixation (20 min, RT), samples were washed twice with PBS (5 min each, RT) and once with 50 mM glycine in PBS (5 min, RT). Blocking and permeabilisation were carried out using 10% FBS with 0.1% Triton X-100 (Sigma) in PBS for 1 h at RT. Primary antibodies were applied at 1:200 dilution in the same blocking/permeabilisation solution and incubated overnight at 4°C. Excess primary antibodies were removed by two washes (5 min each) with the blocking/permeabilisation solution at RT, followed by one wash (5 min, RT) with 1% FBS in PBS. Secondary antibodies were applied at 1:500-1:1000 dilution in 1%

TABLE 1 | List of antibodies used in the study.

Antibody	Manufacturer	Identifiers	Dilutions
Monoclonal anti-LC3A	Sigma/Merck	ZRB1125 clone: 3J12	IF: 1:200
Monoclonal anti-LC3B (rabbit)	Sigma/Merck	ZRB100 clone: 12K5	IF: 1:200 STED: 1:200
Monoclonal anti-CD63 (mouse)	Santa Cruz Biotechnology	MX-49.129.5 clone: sc-5275 RRID:AB_627877	IF: 1:200 STED: 1:200
Goat anti-rabbit Star 580	Abberior	ST580-1002-500UG RRID:AB_2910107	STED: 1:500
Goat anti-mouse Star 635P	Abberior	ST635P-1001-500UG RRID:AB_2893232	STED: 1:500
Monoclonal anti-ATG5 (rabbit)	Sigma/Merck	ZRB1596 clone 1L18	WB: 1:1000
Polyclonal anti-RAB27a (rabbit)	Invitrogen	PA5-79904 RRID:AB_2747019	WB: 1:1000
Polyclonal goat anti-rabbit IgG Fc (HRP)	Abcam	ab97200 RRID:AB_10679899	WB: 1:10000

FBS in PBS for 1 h at RT. Unbound secondary antibodies were removed by two washes (5 min each) with PBS and two washes (5 min each) with distilled water. Details of the antibodies used are provided in Table 1. Samples were mounted in SlowFade Diamond with DAPI (Invitrogen) or ProLong Diamond with DAPI (Invitrogen). For quantification of the cellular microenvironment, images were acquired using an Olympus FluoView FV4000 inverted confocal microscope (EVIDENT) equipped with a 60× oil immersion objective (UPLXAPO60XO, NA 1.42, WD 0.15 mm). Samples were sequentially illuminated with 405, 488, 561 and 647 nm lasers. Images were scanned using galvanometer scanners at 2048 × 2048 pixel resolution. Signals were detected with broadband and red-shifted SilVIR detectors at a dwell time of 2 µs/pixel. Image analysis was performed using ImageJ software.

For multi-channel stimulated emission depletion (STED) nanoscopy SlowFade Diamond Antifade Mountant (Invitrogen) was applied. Imaging was carried out on an Abberior Instruments Facility Line STED microscope system built on an Olympus IX83 fully motorised inverted microscope base. The system was equipped with a ZDC-830 TrueFocus Z-drift compensator, an IX3-SSU ultrasonic stage, a QUADScan beam scanner, avalanche photodiode (APD) detectors and a UPLXAPO60XO 60× oil immersion objective (NA 1.42). Excitation was performed using 488, 561 and 640 nm solid-state lasers, while a 775 nm solid-state laser was used for STED depletion. Image acquisition was controlled using the Imspector data acquisition software (v.16.3.14278-w2129-win64). All other slides were examined using a Leica SP8 Lightning confocal microscope in adaptive lighting mode with a HC PL APO CS2 63×/1.40 oil immersion objective and a hybrid detector. Lookup tables (LUTs) were kept linear throughout the study. Image analysis was performed using Leica LAS X, CellSense FV, Imspector (v.16.3.14278-w2129-win64, Abberior Instruments) and ImageJ software.

2.6 | Modulation of sEV Release by Ca^{2+} Ionophore

Exocytosis of MVEs was induced using the A23187 (Sigma) (Williams et al. 2023). A 1 mM stock solution was prepared in dimethyl sulfoxide (DMSO, Serva). Working solutions at final concentrations of 100, 250, 500 and 1000 nM were made by diluting the stock in fresh, pre-warmed, serum- and antibiotic-free cell culture medium. Cells were treated for 2.5, 5 and 10 min.

In case of quantitative confocal microscopy, the cells and their microenvironment were fixed with 4% PFA. For nanoparticle tracking analysis (NTA), high-resolution flow cytometry and Western blotting, conditioned media were collected. The collected media were centrifuged at 300 *g* for 5 min at RT to eliminate cellular contaminants and then stored on ice until further processing. Chloroquine was used as described previously (Visnovitz et al. 2025).

To monitor the effects of Ca^{2+} ionophore treatment by live-cell imaging, HEK293T cells expressing PalmSORET-CD63GFP-LC3RFP were used. Experiments were performed using a Leica SP8 Lightning confocal microscope equipped with an Okolab environmental chamber. Prior to stimulation, the culture medium was replaced with 50 µL of fresh, pre-warmed, serum- and antibiotic-free medium and image acquisition parameters were established. Final concentrations of the Ca^{2+} ionophore A23187 (100, 250, 500 and 1000 nM) were achieved by adding dissolved ionophore to a final volume of 100 µL immediately before initiation of the experiment. Recording started approximately 30 s after completion of the medium change. Images were acquired every 30 s for a total duration of 10 min. Fluorescence changes were analysed using ImageJ software.

2.7 | Viability Measurements

We used the resazurin assay to evaluate the effect of the Ca^{2+} ionophore on cell viability through mitochondrial metabolic activity (Visnovitz et al. 2025; Koncz et al. 2023). Equal numbers of cells were plated in a 48-well plate (Eppendorf). At 80% confluence, the culture medium was replaced with medium containing the Ca^{2+} ionophore. After the indicated incubation times, the medium was replaced with fresh medium supplemented with FBS, antibiotics and 10 μg/mL resazurin (Sigma). Following 3 h of incubation, the cells were allowed to recover, after which fluorescence changes were measured by Fluoroskan FL fluorometer (Thermo Scientific). To assess the immediate effect of Ca^{2+} ionophore treatment on cell viability, we performed a CellTiter-Glo assay (Promega), which measures cellular ATP levels. Equal numbers of cells were plated into 96-well plate (TPP). Upon reaching 80% confluence, the culture medium was replaced and Ca^{2+} ionophore treatments were applied. At the specified time points, the CellTiter-Glo assay was performed according to the manufacturer's instructions. The final products were transferred to a white plate to minimise background noise. Luminescence was measured using Fluoroskan FL fluorometer (Thermo Scientific) (Szász et al. 2024).

2.8 | Nanoparticle Tracking Analysis (NTA)

Particle concentration and size distribution were determined using a ZetaView PMX120 nanoparticle tracking analysis (NTA) instrument (Particle Metrix) in both scatter and fluorescence modes. Lipophilic EVs were distinguished from non-EV particles using BioxMLYellow (Bioxol), a self-quenchable fluorescent dye (Benke et al. 2023). For fluorescence measurements, samples were labelled with 5 nM dye for approximately 5 min. Instrument settings are provided in Table S1.

2.9 | High Resolution Flow Cytometry

EV secretion from A23187-induced cells was monitored using high-resolution flow cytometry (Apogee Micro-PLUS, Apogee Flow Systems). EVs were identified based on the presence of phospholipid membranes, using BioxMLRed (Bioxol), a lipophilic and self-quenching fluorescent dye, and by their sensitivity to Triton X-100 (Molar Chemicals), as previously described (Koncz et al. 2023; Kovács et al. 2023). A detailed description of the high-resolution flow cytometry settings are provided in Table S2. Data analysis was performed as shown in Figure S2, using FlowJo_V10 software.

2.10 | Holographic Microscopy

Morphometric changes induced by Ca^{2+} ionophore treatment were analysed using a holographic transmission microscope (HoloMonitor M4; Phase Holographic Imaging AB) (Szász et al. 2024, 2025). Changes in cellular morphology, including average cell area, shape irregularity, texture contrast, optical thickness and optical volume, were monitored and quantified. HEK293 cells were cultured and analysed at approximately 60% confluence. Before imaging, the culture medium was replaced with 3 mL of serum-free medium, either containing 500 nM Ca^{2+} ionophore or without ionophore (control). Time-lapse images were acquired every 10 s for 10 min. For image analysis, at least 70 cells per field of view were identified using the minimum error histogram-based thresholding algorithm implemented in the built-in software (HStudio M4).

2.11 | Gene Silencing

ATG5 and RAB27a genes were silenced in HEK293 and HEK293T-PalmGFP-LC3RFP cells using pre-designed Silencer Select siRNAs (Ambion). Transfections were performed using Lipofectamine RNAiMAX (Invitrogen) according to the manufacturer's protocol with minor modifications. Cells were maintained in antibiotic-free DMEM until they reached 30%–50% confluence. RNAi duplex-Lipofectamine RNAiMAX complexes were prepared in serum- and antibiotic-free Opti-MEM medium (Gibco) at a final siRNA concentration of 10 nM. After 4–6 h of transfection, 10% FBS was added to the medium, and cells were incubated for an additional 3 days. Subsequently, the medium was replaced with fresh siRNA-containing Opti-MEM, and FBS was reintroduced after 4–6 h. Cells were cultured for one more day before being used in experiments. The sequences of the siRNAs are provided in Table 2.

2.12 | Quantitative Real-Time PCR

To assess gene silencing at the RNA level, quantitative real-time PCR (qPCR) was performed. PCR primers were designed using Primer3web (https://primer3.ut.ee/) and validated on a Kyratec SC300T PCR system (Kyratec) followed by agarose gel electrophoresis. Sequences of the PCR primers are listed in Table 3. Total RNA was extracted from HEK293 cells using the NucleoSpin RNA Plus Kit (MACHEREY-NAGEL) according to the manufacturer's instructions. Cells were cultured in 6-well plates (VWR) or T12.5 flasks (VWR). After mechanical detachment, cells were collected by centrifugation at 300 *g* for 5 min at RT. Pellets were lysed in the provided lysis buffer, and RNA was eluted in 30 μL of RNase-free water. RNA content and purity were determined using a NanoDrop-1000 spectrophotometer (Thermo Fisher Scientific). The reverse transcription was performed using 1 μg of total RNA and an $Oligo(dT)_{18}$ primer with the RevertAid First Strand cDNA Synthesis Kit (Thermo Fisher Scientific), following the manufacturer's protocol. The qPCR was carried out using 20 ng of cDNA, 3–5 pmol of each primer and SensiFAST SYBR Hi-ROX Mix (BioLine) on a CFX96 Touch Real-Time PCR System (Bio-Rad). Data were analysed using CFX Maestro software (Bio-Rad). The amplification protocol is summarised in Table 4. Gene expression levels were normalised to the housekeeping gene GAPDH.

2.13 | Western Blotting

Western blotting was performed as described previously (Visnovitz et al. 2025; Koncz et al. 2023). Whole-cell lysates were analysed to assess silencing efficiency at the protein level. Cells were cultured in T25 flasks (Eppendorf) until reaching approximately 80% confluence. After mechanical detachment,

TABLE 2 | Nucleotide sequences of applied siRNAs.

siRNA ID #	Senquence	Target gene:	Locus ID:
s18160	5′ GCU AUA UCA GGA UGA GAU Att 3′ 3′ tg CGA UAU AGU CCU ACU CUA U 5′	ATG5 Hs.486063	9474
s11693	5′ GCC UCU ACG GAU CAG UUA Att 3′ 3′ ta CGG AGA UGC CUA GUC AAU U 5′	RAB27A Hs.626665	5873

TABLE 3 | List of PCR primers.

Target gene	Forward primer sequence 5′→3′	Reverse primer sequence 5′→3′
GAPDH	CCTCCTCACAGTTGCCATGTA	TGGTTGAGCACAGGGTACTTT
ATG5	GAAGCTGTTTCGTCCTGTGG	CCGGGTAGCTCAGATGTTCA
RAB27a	GAAGCCATAGCACTCGCAGAGA	CAGGACTTGTCCACACACCGTT

TABLE 4 | Thermal profile of qPCR reactions.

Amplification		
Set temperature	**Time**	**Number of cycles**
95°C	1 min	1
95°C	30 s	40
60°C	1 min	
72°C	5 min	1
Melting curve		
Set temperature	**Steps**	**Number of cycles**
65°C→95°C	0.5°C	1
4°C		∞

cells were harvested by centrifugation at 300 *g* for 5 min at RT. Pellets were lysed in radio-immunoprecipitation assay (RIPA) buffer supplemented with 1 mM PMSF (Serva) and 2 mM sodium orthovanadate (Sigma). For analysis of the extracellular environment, total protein from conditioned, serum- and antibiotic-free medium was precipitated using trichloroacetic acid (TCA) as described previously (Koncz et al. 2023; Koontz 2014) with minor modifications. After removing cells by centrifugation (300 *g*, 10 min, RT), proteins were precipitated on ice for at least 1 h. Precipitated proteins were collected by centrifugation at 20 000 *g* for 20 min at 4°C, then washed twice with −20°C acetone. Protein pellets were resuspended in RIPA buffer as described above. Protein concentrations were determined using the Micro BCA Protein Assay Kit (Thermo Fisher Scientific) and a MULTISKAN SkyHigh Microplate Spectrophotometer (Thermo Fisher Scientific).

Proteins were separated on 12% polyacrylamide gels (acrylamide/bis-acrylamide ratio 37.5:1) using a Mini-PROTEAN system (Bio-Rad). For improved solubilisation of membrane proteins, equal volumes of 0.1% Triton X-100, Laemmli buffer, and samples were mixed as described previously (Visnovitz et al. 2012). Within each biological replicate, equal amounts of protein (~15–20 μg) were loaded per lane. After electrophoresis, proteins were transferred to PVDF membranes (Serva). Membranes were blocked with 5% BSA in TBS-T for 1 h at RT. Primary antibodies and their dilutions are listed in Table 1. Peroxidase-conjugated secondary antibodies were applied at 1:10 000 dilution. Signals were detected using ECL Western Blotting Substrate (Thermo Scientific) and visualised with an Imager CHEMI Premium system (VWR).

2.14 | Proteomics

Total protein content of serum- and cell-free conditioned media was analysed. The proteins were precipitated as previously described (Koncz et al. 2023). Protein samples were re-dissolved in 20 μL of 8 M urea in 50 mM ammonium bicarbonate solution. Then, 0.5 μL of 200 mM dithiothreitol was added, incubated at 37°C for 30 min, followed by the addition of 1.1 μL of 200 mM iodoacetamide and incubation at RT in the dark for 30 min. Protein concentration was determined using the Lowry assay with bovine serum albumin as a calibration standard. Next, 10 μg of protein from each sample was diluted to 30 μL with 50 mM ammonium bicarbonate. Proteins were digested by adding 100 ng

LysC-trypsin and incubating at 37°C for 1 h, followed by the addition of 1 μg trypsin and further incubation at 37°C for 15 h. Digestion was quenched by adding 0.5 μL formic acid (FA), after which samples were dried and purified by Pierce C_{18} (Thermo Fisher Scientific) solid-phase extraction.

Briefly, cartridges were washed with 2 × 200 μL 50% methanol, 2 × 200 μL 0.5% trifluoroacetic acid (TFA) in 5% acetonitrile (ACN) and 2 × 200 μL 0.1% TFA. Samples were loaded in 50 μL of 0.1% TFA, and reloaded once, then washed with 2 × 100 μL 0.1% TFA and eluted with 2 × 50 μL 0.1% TFA in 70% ACN. Each step was followed by centrifugation at 2500 *g* for 2 min. Finally, samples were dried down and stored at −20°C.

Proteomic samples were dissolved in 0.1% FA with 0.15% dodecyl-*β*-D-maltoside solution, and 100 ng of peptides was injected from each sample. Samples were analysed on a timsTOF HT coupled with a nanoElute 2 system (Bruker Daltonics). Samples were first loaded onto an Inertsil ODS-4 trap column (C_{18}-coated particles, 3 cm) at a flow rate of 10 μL/min, followed by separation on a Bruker PepSep Advanced C_{18} analytical column (75 μm × 250 mm, 1.5 μm particles, 100 Å pores) maintained at 50°C. Eluent A consisted of 0.1% FA in water, while eluent B was 0.1% FA in 100% ACN. The gradient started at 5% B and increased to 35% B over 26 min at a flow rate of 0.3 μL/min.

A *CaptiveSpray* 1 ion source was used in positive mode at a capillary voltage of 1500 V. A mass range of m/z 100–1700 and an ion mobility range of 0.7–1.4 V·s/cm^2 were applied. To establish optimal acquisition conditions, initial measurements were performed in data-dependent parallel accumulation-serial fragmentation (PASEF) mode, and the resulting data were used to generate a spectral library in FragPipe. Based on this library, data-independent analysis (DIA) windows were optimised using py_diAID (Skowronek et al. 2022), followed by DIA-PASEF analysis of all samples. Accumulation and ramp times were both set to 180 ms, while transfer and prepulse storage times were set to 60 and 12 μs, respectively. Four DIA-PASEF MS/MS events were recorded per cycle, resulting in a cycle time of 0.93 s, with MS1 spectra acquired within each cycle.

Precursor ions with charge states up to 5 were considered, using an inclusion threshold of 1500 and a target intensity of 15 000. Dynamic exclusion was applied with a release time of 0.4 min, precursor reselection was enabled and a current-to-previous intensity ratio of 4 was applied. Exclusion tolerances were set to 0.015 *m/z* in the mass dimension and 0.015 V·s/cm^2 in the ion mobility dimension.

Protein identification and quantification were carried out using DIA-NN (Demichev et al. 2020), searching against the UniProt human database with trypsin/P specificity. Carbamidomethylation of cysteine residues was set as a fixed modification, while *N*-terminal methionine excision, methionine oxidation and protein *N*-terminal acetylation were included as variable modifications. A maximum of one variable modification and one missed cleavage were permitted.

Statistical evaluation and data visualisation were performed using custom scripts in R within RStudio. Proteins identified with at least two unique peptides and quantified in more than half of the samples in at least one sample group were retained. When a protein was detected in less than two-thirds of the samples within a group, values were imputed using the fifth percentile of the respective sample distribution. Otherwise, missing values were imputed using the *k*-nearest neighbours method ($k = 15$) implemented in the VIM package (Kowarik and Templ 2016).

Differential expression analysis was performed on log-transformed intensities using the limma package (Ritchie et al. 2015) with empirical Bayes moderation. Pairwise contrasts between experimental groups were evaluated, and *p* values were adjusted for multiple testing using the Benjamini–Hochberg method. Proteins with an adjusted p value < 0.05 were considered significant.

For proteins exhibiting global differences across samples ($n = 81$ proteins), principal component analysis (PCA) and hierarchical clustering using the Ward.D2 method were performed. A heat map was generated from *Z*-score-scaled data. Gene Ontology (GO) Cellular Component annotations were used to classify the identified proteins according to their subcellular localisation.

2.15 | Figures and Statistical Analysis

Figures and graphs were generated using GraphPad Prism version 9.4.1, BioRender (BioRender.com), FlowJo_V10 and Microsoft Office 2016. Statistical analyses were performed using GraphPad Prism version 9.4.1. Statistical significance was defined as $^{*}p < 0.05$, $^{**}p < 0.01$, $^{***}p < 0.001$ and $^{****}p < 0.0001$.

3 | Results

3.1 | Identification of MV-lEVs in Different Mouse Tissues

In our very recent study, we demonstrated the presence of large multivesicular extracellular vesicles (MV-lEVs) in various cell lines as well as in mouse kidney and liver. In many cases, we confirmed that these MV-lEVs represent a novel EV subtype of amphisomal origin, and we termed them amphiectosomes (Visnovitz et al. 2025). First, we addressed the question of whether MV-lEV secretion is a general process, which can be observed in different organs and tissues of a complex organism such as the mouse. Ultrathin sections of mouse spleen (Figure 1A–C), lungs (Figure 1D,E), skeletal muscle (Figure 1F,G), heart (Figure 1H,I), small intestine (Figure 1J–L), kidney (Figure 1M) and liver (Figure 1N,O) were examined by transmission electron microscopy. MV-lEVs were detected in all analysed tissues. Furthermore, different stages of MV-lEV secretion were observed, including budding (Figure 1A,E,H,O), intact MV-lEVs in the extracellular space (Figure 1B,D,F,G,I,K,N) and release of intraluminal vesicles (Figure 1C,J,M). Thus, the characteristic 'torn bag mechanism' was clearly visible in all the tested tissues and organs. In agreement with our previous findings, under steady state conditions, secretion of MVEs by exocytosis was essentially not detected. In small intestine, however, secretion of sEVs via ectocytosis was observed (Figure 1L), where sEVs were released from microvilli.

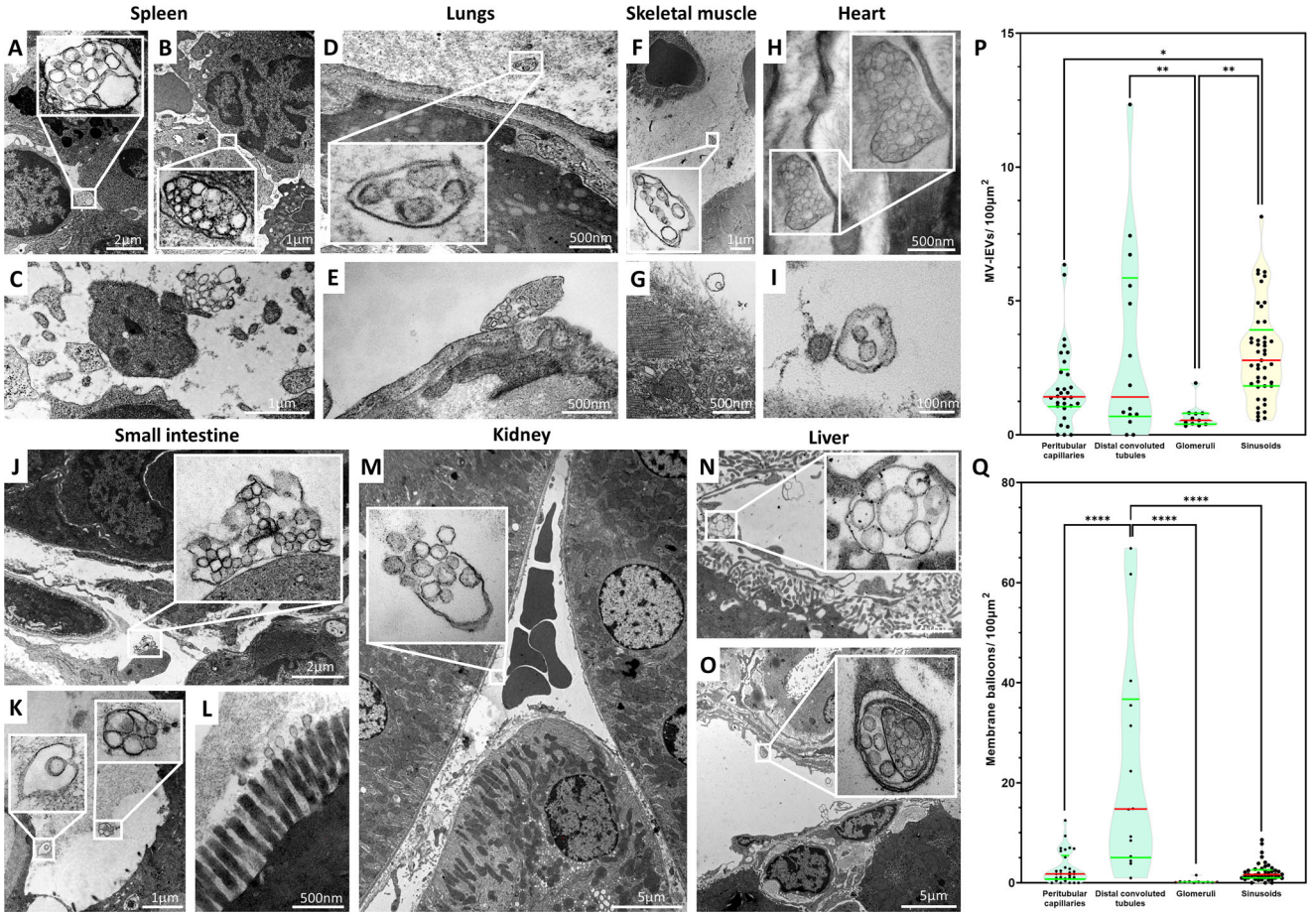

FIGURE 1 | MV-lEVs in mouse organs and tissues. Transmission electron microscopy revealed MV-lEVs in spleen (A–C), lungs (D, E), skeletal muscle (F, G), heart (H, I), small intestine (J–L), kidney (M) and liver (N, O). Stages of MV-lEV secretion were observed, such as budding (A, E, H, O), intact MV-lEVs in the extracellular environment (B, D, F, G, I, K, N) and release of intraluminal vesicles (C, J, M). Under steady-state conditions, secretion of MVEs by exocytosis was not detected, while sEV secretion via ectocytosis occurred in the small intestine (L). Frequency of any forms of MV-lEVs (P) and large empty membrane balloons (>300 nm in diameter; Q) was determined in the kidney (green) and liver (yellow). MV-lEV frequency did not differ between peritubular capillaries and distal convoluted tubules. When normalised to surface area, MV-lEV frequency decreased in kidney glomeruli but increased in liver sinusoids compared to kidney distal convoluted tubules. The density of large membrane balloons did not differ between kidney peritubular capillaries and liver sinusoids; however, distal convoluted tubules contained significantly more membrane balloons. In kidney glomeruli, large membrane balloons were very rare. Three independent ultrathin sections per organ were evaluated. Statistical significance was assessed using one-way ANOVA with Tukey's multiple comparisons post hoc test (*$p < 0.05$, **$p < 0.01$, ***$p < 0.001$, ****$p < 0.0001$). p values are available in Figure S1 statistics.xlsx.

To assess the prevalence of MV-lEV secretion in murine kidney and liver, the frequencies of MV-lEVs and large empty membrane balloons (>300 nm in diameter) were quantified in distinct tissue compartments (Figure 1P,Q). MV-lEV secretion was found to be a common phenomenon in both mouse kidney and liver, with couple of detected MV-lEVs per 100 µm^2. The density of empty membrane balloons was comparable with the occurrence of MV-lEV, except in kidney glomeruli, where presence of membrane balloons was rare. MV-lEV frequency did not differ between kidney peritubular capillaries and distal convoluted tubules. However, MV-lEV number was reduced in kidney glomeruli, whereas a significant increase was observed in liver sinusoids compared with kidney peritubular capillaries (Figure 1P). In contrast, the density of large empty membrane balloons was similar between kidney peritubular capillaries and liver sinusoids, while distal convoluted tubules contained a significantly higher number of these structures. Large membrane balloons were rarely detected in kidney glomeruli (Figure 1Q).

3.2 | Effect of Ca^{2+} Ionophore on EV Secretion

To investigate the effect of Ca^{2+} ionophore on EV secretion, HEK293 cells were exposed to increasing concentrations of A23187 and analysed by TEM, NTA and high-resolution flow cytometry (Figure 2). Under steady state control conditions and at A23187 concentrations below 250 nM, the predominant sEV release pathway seemed to be the 'torn bag mechanism', whereas MVE exocytosis was hardly detectable (Figure 2A-I,X,Z). TEM revealed distinct stages of MV-lEV secretion, including plasma membrane budding, intact MV-lEVs in the extracellular space, release of intraluminal vesicles and empty limiting membrane balloons (Figure 2A-I). These features were consistently observed

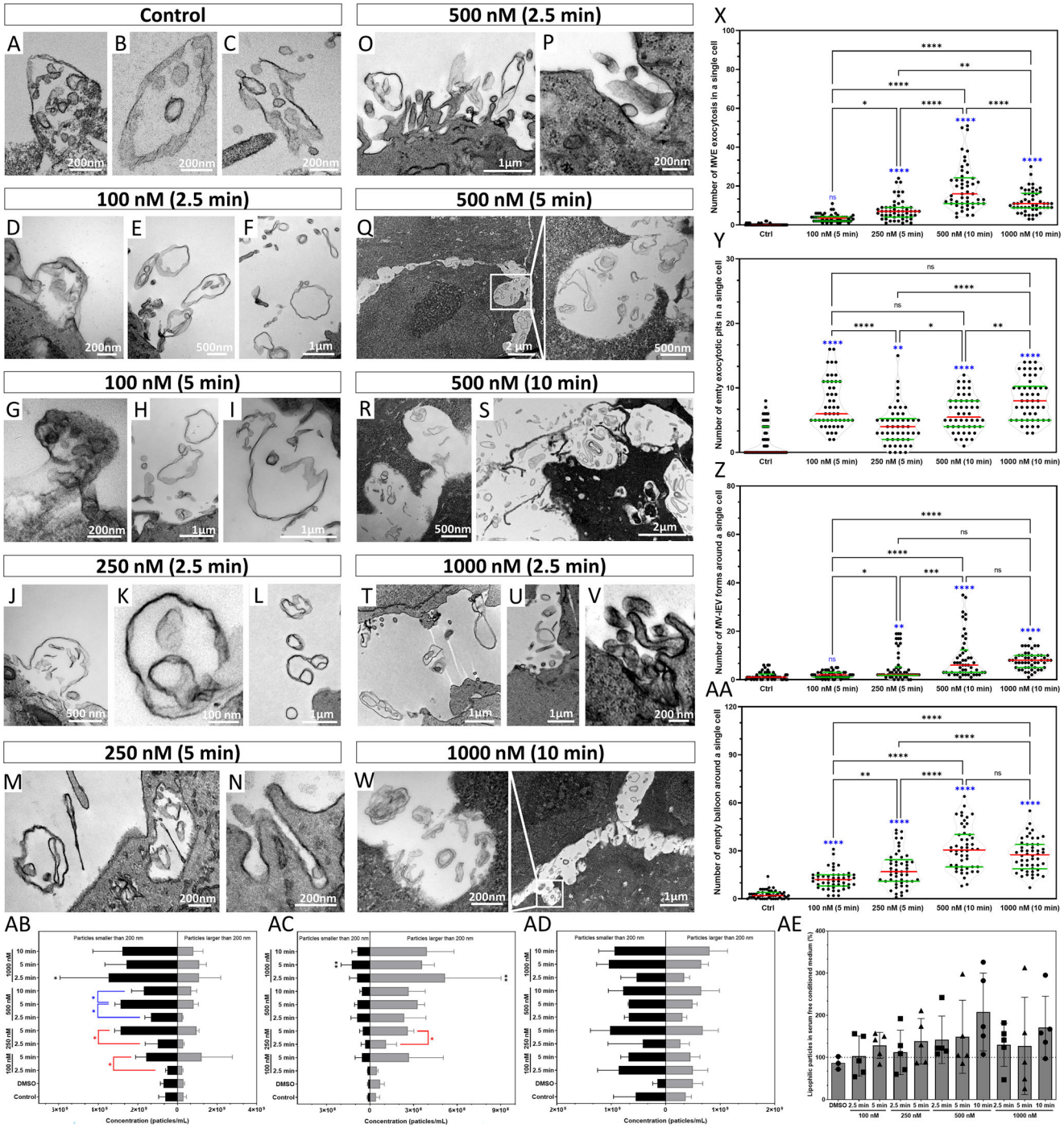

FIGURE 2 | Legend on next page.

across three different samples on multiple fields, confirming that MV-lEV secretion is continuously present under these conditions.

Importantly, at 250 nM A23187 for 5 min, we detected significant increase in MVE exocytosis (Figure 2N,X) in addition to MV-lEV secretion and the 'torn bag mechanism', which frequency also slightly increased (Figure 2M,Z). With further increase in Ca^{2+} ionophore concentration and treatment duration, MVE exocytosis became the dominant sEV release mechanism (Figure 2O-X,Z). Mean frequency of MV-lEV was approximately half of the frequency of MVE exocytosis in a single cell at 500 nM ionophore treatment. Of note, at higher A23187 concentrations, both MV-lEV secretion (Figure 2O,T) and MVE exocytosis (Figure 2P,U,V) were observed at early time points (2.5 min), whereas at later stages (5–10 min), mainly MVE exocytosis and large empty membrane balloons were detected (Figure 2Q-S,W), only ruptured MV-lEVs were present. The empty membrane balloons may originate from the limiting membranes of these structures.

For quantitative analysis of Ca^{2+} ionophore-dependent particle release, NTA and high-resolution flow cytometry were performed, testing cell-free supernatant diluted in PBS. NTA in scatter mode revealed a significant, concentration- and time-dependent increase in both small (<200 nm, Figure 2AB) and

larger (>200 nm, Figure 2AC) particles up to 1000 nM A23187. At 1000 nM A23187 concentration, no further increase was observed in particle counts, suggesting a saturation effect. Interestingly, when lipophilic fluorescent labelling was applied, no significant increase in fluorescence was detected, although a slight trend was observed (Figure 2AD). The discrepancy between scatter and fluorescence modes suggests that a substantial fraction of released particles may lack a limiting membrane. Median (X50) sizes of particles in the supernatant are indicated in Figure S1. These findings were further supported by high-resolution flow cytometry. Although an increasing trend in EV release was observed by fluorescent membrane labelling, it did not reach statistical significance (Figure 2AE). Overall, Ca^{2+} ionophore treatment significantly enhances the release of extracellular particles in a dose-dependent manner; however, only a subset of these particles appears to be real EVs. Gating strategy of high-resolution flow cytometry for EV detection is found in Figure S2.

3.3 | Characterisation of Ca^{2+} Ionophore-Induced EV Secretion

To investigate the nature of the EVs released by the effects of Ca^{2+} ionophore, we tested HEK293T-PalmGFP and HEK293T-PalmSORET-CD63GFP-LC3RFP cells. We employed a combination of immunocytochemistry and live cell imaging by confocal microscopy, STED super-resolution microscopy and holographic microscopy. By immunocytochemistry EV subtypes were characterised and quantified based on PalmGFP plasma membrane, CD63 and LC3B protein markers. Representative confocal images, which were used for quantification, are shown in Figure 3A-D. The results reveals distinct changes in EV subpopulations following Ca^{2+} ionophore (A23187) treatment. PalmGFP fluorescence, indicating plasma membrane-derived EVs, fluctuated around control levels with minor but significant changes. Prominent plasma membrane derived EV release was detected at 500 nM ionophore between 2.5 and 5 min timepoints (Figure 3E). In contrast, CD63-positive EVs exhibited pronounced time- and concentration-dependent responses. At 2.5 min, CD63 signal continuously increased and reached saturation at 500 nM. Similar a trend was recognised at 5 min time points. Following the effect of concentration dependency, at lower concentrations (100–250 nM) CD63 fluorescence continued to increase over time, whereas at higher concentrations (500–1000 nM), a significant decrease occurred at 10 min time points (Figure 3F). The LC3B-positive EVs followed a pattern similar to PalmGFP, with an extra peak at 250 nM and 5 min. A slight and concentration-dependent increase was observed at 2.5 min, which plateaued at a 500 nM Ca^{2+} ionophore concentration. At higher concentrations of A23187 (500–1000 nM), a decreasing time-dependent trend was found (Figure 3G).

Live-cell confocal microscopy was performed on HEK293T-PalmSORET-CD63GFP-LC3RFP cells to support the quantitative imaging data obtained on fixed cells (Figure 3H-L). Due to dilution of EVs in the extracellular space, fluorescence changes of released particles could not be directly detected, therefore, intracellular fluorescence levels were followed as an indicator for EV secretion. A decrease in the intracellular fluorescent signal may interpreted as vesicle release. Under control conditions and 100 nM A23187 treatment, intracellular PalmSORET, CD63-GFP, and LC3-RFP fluorescence intensities fluctuated around baseline without significant temporal changes (Figure 3H,I). In contrast, higher ionophore concentrations (250, 500, and 1000 nM) resulted in a time- and concentration-dependent reduction of intracellular fluorescence signals (Figure 3J-L), consistent with enhanced vesicle secretion. Notably, at the 5-min time point following 250 and 500 nM A23187 treatment, a transient increase in CD63-GFP signal was observed concomitantly with a decrease in LC3-RFP intensity. Analysis of LC3B-positive EV secretion in fixed cells revealed a similarly robust autophagy-derived EV release at the 5 min time point following 250 nM A23187 treatment, consistent with observations from live-cell imaging.

STED imaging confirmed that at least a subset of released MV-lEVs were amphiectosomes containing CD63- and LC3B-positive intraluminal vesicles (Figure 3M,N). Intact amphiec-

FIGURE 2 | Effect of Ca^{2+} ionophore on EV secretion. The impact of A23187 Ca^{2+} ionophore treatment on HEK293 cells was assessed using transmission electron microscopy (A-AA), nanoparticle tracking analysis (NTA; AB-AD) and high-resolution flow cytometry (AE). Under control conditions (A–C) and at 100 nM A23187 concentrations (D–I), the predominant sEV secretion pathway was the 'torn bag mechanism'. Multivesicular endosome (MVE) exocytosis was observed only after 5 min of treatment with 250 nM A23187 (N). Stages of MV-lEV secretion included budding (A, D, G, J), intact MV-lEVs in the extracellular space (B, E, K, M), release of intraluminal vesicles (C, I) and empty limiting membrane balloons of MV-lEVs (E, F, H, L) were recorded. The number of MVE exocytosis events (X), exocytotic pits (Y), MV-lEVs surrounding a cell (Z) and empty membrane balloons (AA) were quantified. In control (Ctrl) cells, MVE exocytosis was an extremely rare event; however, its frequency increased with rising A23187 concentrations and reached saturation at 500 nM (X). A similar concentration-dependent trend was observed for large empty membrane balloons (AA). In the case of empty exocytotic pits, an ionophore-dependent increase was detected, although a clear concentration-dependent relationship was not observed (Y). The number of all MV-lEVs (including ruptured MV-lEVs with visible ILVs) showed a moderate increase with A23187 concentration and reached a plateau above 500 nM (Z). NTA was applied to quantify particle release in scatter mode for sEV (AB) and lEV (AC) settings and in fluorescence mode (AD). In scatter mode, both small (<200 nm; AB) and larger (>200 nm; AC) particle numbers increased significantly in a concentration- and time-dependent manner up to 1000 nM A23187 concentration. No further time-dependent increase was detected at 1000 nM A23187. When a lipophilic fluorescent dye (BioxML-Yellow) was applied, this significant increase was not observed in fluorescence-mode NTA (AD). Findings were further validated by high-resolution flow cytometry (AE). Statistical significance was determined by one-way ANOVA completed by Tukey's multiple comparisons post hoc test or Dunnett's multiple comparisons test. In case of quantitative TEM (X-AA), three independent biological replicates were analysed on 3–5 ultrathin sections. Blue symbols indicate the comparison between treated cells and Ctrl. In case of NTA (AB-AD) and high-resolution flow cytometry (AE), in addition to the one-way ANOVA completed by Dunnett's multiple comparisons tests (black symbols) within treatments, Student's *t*-test (red symbols) or ANOVA with Tukey's multiple comparisons post hoc test (blue symbols) were used. Error bars represent the mean ± SD of 3 (AB-AC), 4 (AD) and 3–5 (AE) biological replicates, respectively (*$p < 0.05$, **$p < 0.01$). *p* values are available in Figure S2 statistics.xlsx.

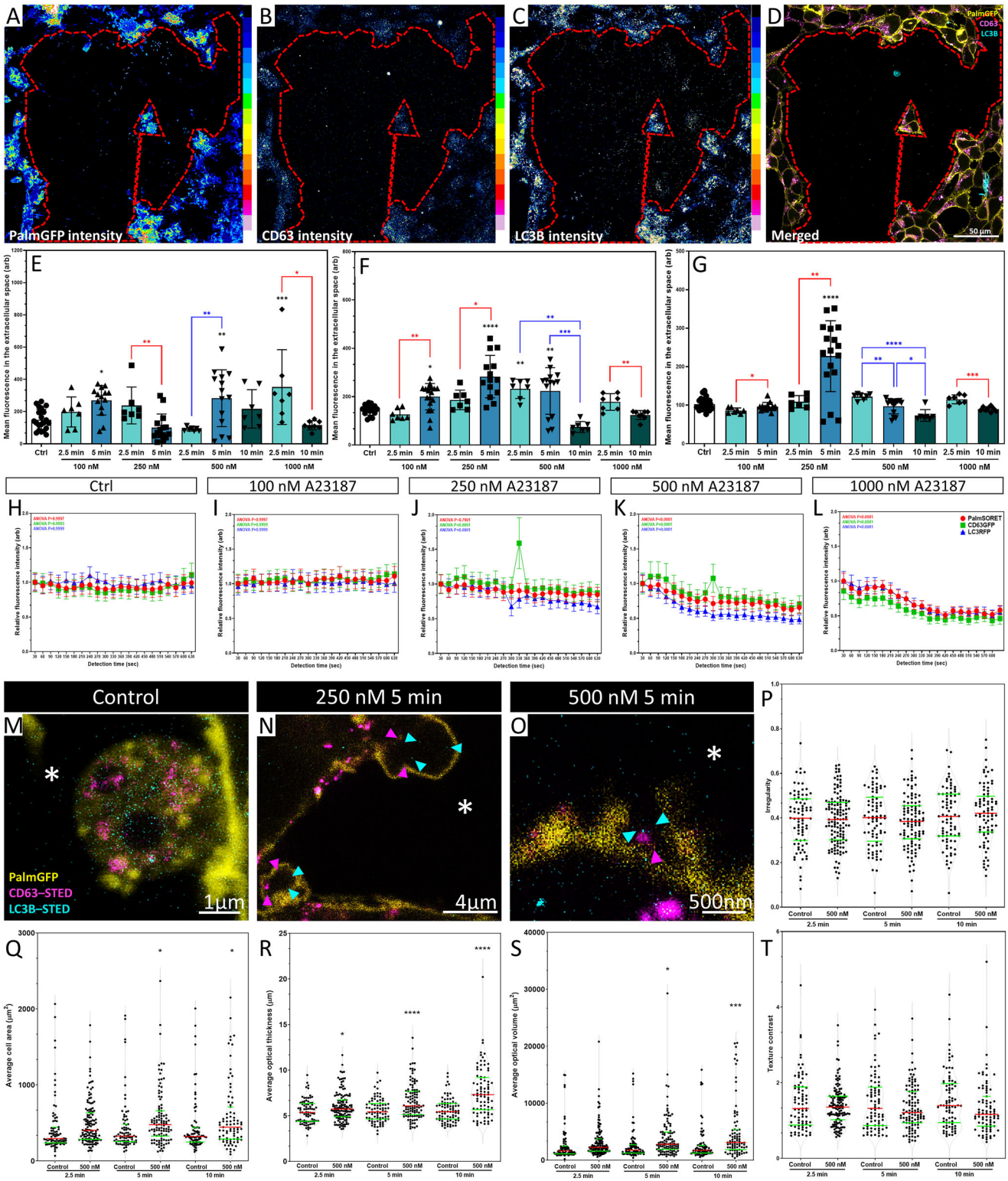

FIGURE 3 | Legend on next page.

tosomes were not found after 5 min at 500 nM ionophore, although evidence of amphisome exocytosis was observed (Figure 3O).

Cellular morphology and integrity were assessed during ionophore treatment using holographic microscopy. Morphometric analysis indicated that cellular irregularity and texture contrast remained unchanged during the Ca^{2+} ionophore treatments (Figure 3P,T), while average cell area, average optical thickness and average optical volume increased significantly in a time-dependent manner (Figure 3Q-S).

The effect of A23187 treatments on HEK293 cells' viability was followed by two different assays (resazurin assay and CellTiter-

Glo). Based on the resazurin assay, the treatments did not significantly change the viability (Figure S3A), while in CellTiter-Glo assay at 1000 nM A23187 concentration (10 min) a significant drop of the ATP level was recorded (Figure S3B), indicating that the treatment affects the cells' metabolic activity, but within 3 h the cells were able to recover.

3.4 | Further Characterisation of A23187-Induced Secretion in HEK293 Cells

As NTA and high-resolution flow cytometry indicated, only a subset of the released particles represented membrane-enclosed EVs therefore, further ultrastructural and molecular characterisation was performed. Quantitative TEM analysis of EV- and particle-enriched pellets revealed that under control conditions, the majority of secreted vesicles were small EVs (sEVs; <200 nm), with only occasional lysosome-derived electron-dense particles and rare damaged mitochondrion-derived structures (Figure 4A-C). In contrast, Ca^{2+} ionophore treatment induced pronounced qualitative and quantitative changes in the secreted particle population. Increasing concentrations of A23187 (250 and 500 nM) led to an increased abundance of lysosome-derived and mitochondrion-derived particles (Figure 4D-I), accompanied by the appearance of ruptured MV-lEVs at 500 nM (Figure 4G). Vesicle size analysis demonstrated a concentration-dependent shift toward larger vesicles (Figure 4J), with a significant increase in the proportion of large EVs (lEVs; >200 nm) upon A23187 treatment (Figure 4K). Although the abundance of lysosome- and mitochondrion-derived particles was significantly elevated compared with control conditions, their levels reached a plateau, showing no significant difference between the 250 and 500 nM treatments (Figure 4L,M).

In parallel, mass spectrometry-based whole secretome analysis identified 4713 proteins across all conditions, with the majority detected in both control and treated samples. Notably, 120 proteins were uniquely identified following Ca^{2+} ionophore treatment (Figure 4N). Of these, 108 proteins were present in the secretome of cells treated with 250 and 500 nM A23187, but absent under control conditions. Table 5 provides the Gene Ontology (GO) classification of these proteins together with selected EV-associated proteins. The complete protein list is available in Supporting Information Mass Spectrometry Data of Secretome.xlsx. The secretome related findings are consistent with the TEM observations, indicating that ionophore-induced stress promotes the release of lysosome- and mitochondrion-derived particles as well as large membrane-enclosed EVs. Quantitative proteomic analysis identified 81 proteins with significantly altered abundance. Both principal component analysis (Figure 4O) and hierarchical clustering heat map analysis of these differentially expressed proteins (Figure 4P) revealed a clear separation between control and ionophore-treated groups, confirming distinct treatment-induced alterations in secreted vesicles, particles and released proteins.

3.5 | Modulation of sEV Release Pathways

To investigate the contribution of the 'torn bag mechanism' and MVE exocytosis-based sEV release pathways, we combined ultrastructural analysis with targeted gene silencing and chemical modulation of either the 'torn bag mechanism' or MVE exocytosis. Under steady state conditions, TEM revealed that the predominant mechanism of sEV release might be the 'torn bag' pathway (Figure 5A,B), whereas MVE exocytosis was not detected. Interestingly, starvation of cells in serum-free cell

FIGURE 3 | Characterisation of Ca^{2+} ionophore-induced EV secretion. The mechanism and the quantity of Ca^{2+} ionophore-induced EV secretion were evaluated in HEK293T-PalmGFP cells using immunocytochemistry combined with quantitative confocal microscopy (A–G) and STED super-resolution microscopy (M–O). Mean fluorescence intensities of PalmGFP (A, E), CD63 (B, F) and LC3B (C, G) were determined in the extracellular environment. The coverslip surface (where EVs were trapped within the gelatin-fibronectin coating) is shown in representative intensity images (A–C), and a merged composite image of the cells in Panel D. The extracellular space, indicated by a red dashed line (A–D) was selected based on the location of the HEK293T-PalmGFP cells (D). The analysis revealed that the concentrations of GFP-positive (plasma membrane-derived) EVs fluctuated around control levels, with some significant differences (E), whereas CD63-positive EVs followed a time- and concentration-dependent dynamics. After 2.5 min of treatment, CD63-positive EV concentrations gradually increased and saturated at 500 nM A23187. A similar trend was observed at 5 min. At 100 and 250 nM A23187 treatments, CD63-dependent fluorescence increased over time, while at 500 and 1000 nM, the opposite effect occurred. After 10 min, the signal significantly dropped (F). LC3B-positive EVs showed a pattern similar to PalmGFP-positive EVs with an additional peak at 250 nM and 5 min. At 2.5 min, a slight concentration-dependent increase was observed with saturation at 500 nM A23187 (G). To determine the secreted particle identities and molecular changes intracellularly, HEK293T-PalmSORET-CD63GFP-LC3RFP cells were followed with confocal microscopy during Ca^{2+} ionophore treatments (H–L). Under control conditions (H) all the fluorescent intensities fluctuated around the mean value without any significant changes. Similar results were recorded in case of 100 nM A23187 treatment (I). In the case of higher concentration 250 nM (J), 500 nM (K) and 1000 nM (L) the intracellular fluorescent signals decreased in a time a concentration dependent way. At 5 min timepoints of 250 nM and 500 nM a clear increase is visible in the intracellular GFP signal together with a drop in the RFP. STED microscopy provided evidence that at least a subset of released MV-lEVs were amphiectosomes containing CD63- and LC3B-positive intraluminal vesicles (M, N). Following 500 nM A23187 treatments for 5 min, intact amphiectosomes were not observed; however exocytosis of amphisomes were detected (O). White asterisks indicate the extracellular environments during the STED analysis. CD63 (magenta) and LC3B (cyan) were super-resolution channels while GFP (yellow) was a confocal channel. Cellular morphology and integrity were assessed during ionophore treatments of HEK293 cells using holographic microscopy. Cellular irregularity (P) and texture contrast (T) remained unchanged, while average cell area (Q), optical thickness (R) and optical volume (S) increased in a time-dependent manner based on quantification of 80–129 cells. Error bars represent mean ± SD (E–G) or mean and 95% CI (H–L). Statistical significance was determined in case of subfigure E–G between control and treated conditions by one-way ANOVA followed by Dunnett's multiple comparisons test (black symbols). Within treatment groups Student's t-test (red symbols) and one-way ANOVA with Tukey's post hoc test (blue symbols) was performed. In case of live cell imaging one-way ANOVA with Dunnett's test was applied, while for analysis of comparison between control an treated cells during holographic microscopy Student's *t*-test was used (*$p < 0.05$, **$p < 0.01$, ***$p < 0.001$, ****$p < 0.0001$). *p* values are available in Figure S3 statistics.xlsx.

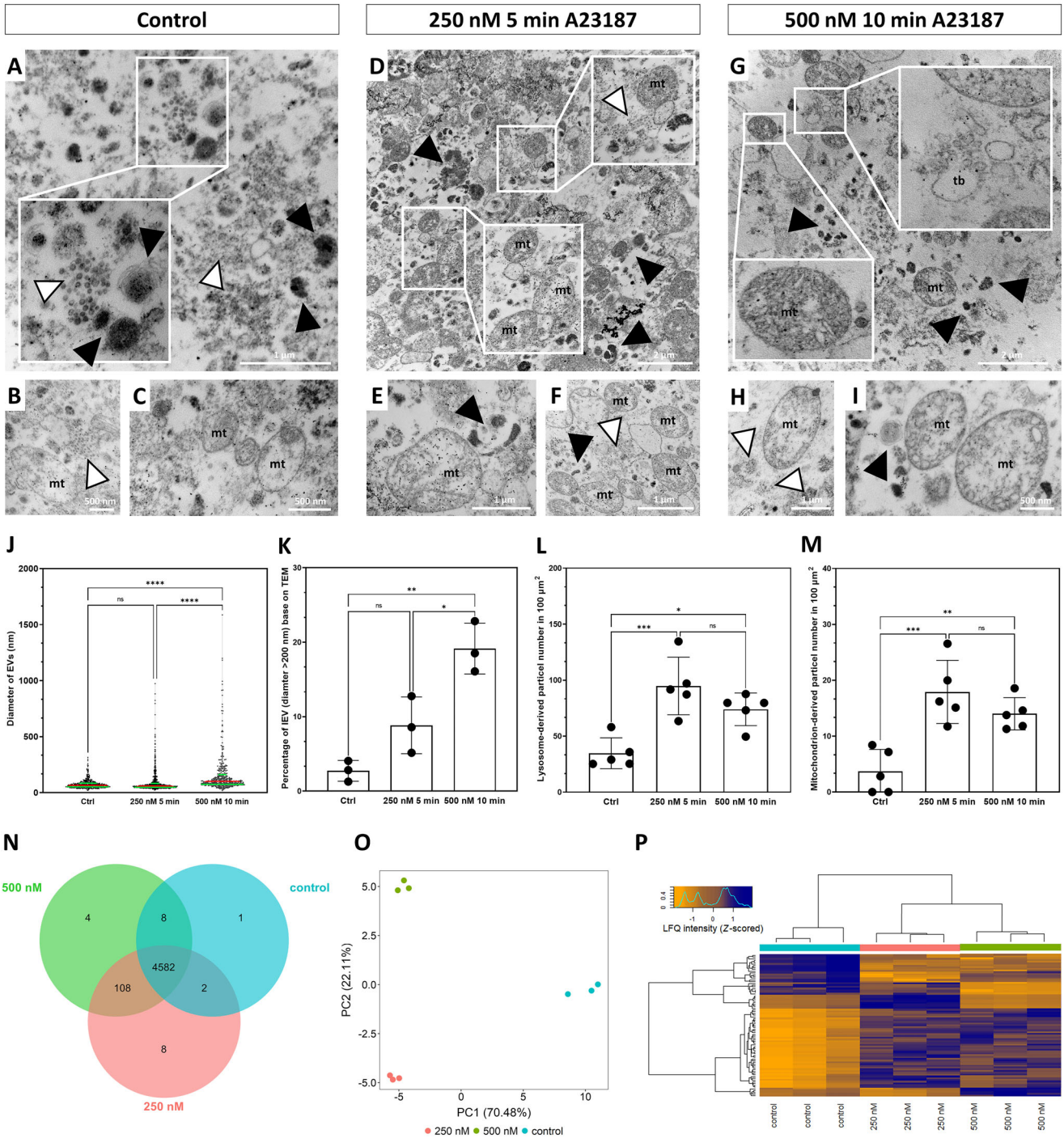

FIGURE 4 | Legend on next page.

culture medium (a condition commonly used in the EV field [Théry et al. 2018]), elicited a dual response: while the 'torn bag mechanism' persisted (Figure 5C), MVEs accumulated in the cytoplasm (Figure 5E) and fused with the plasma membrane, indicating activation of the exocytosis pathway (Figure 5D,F).

To further explore the relationship between the 'torn bag mechanism' and MVE exocytosis, we silenced RAB27a (Ostrowski et al. 2010), a key regulator of MVE docking and fusion, and ATG5, an essential component of autophagosome biogenesis through phagophore membrane formation (Klionsky et al. 2021) (Figure 5G). RAB27a knockdown abolished MVE exocytosis (Figure 5H,I), even under calcium ionophore (A23187) stimulation (Figure 5M), forcing cells to rely on the 'torn bag mechanism' for sEV release (Figure 5J,N). In contrast, in the absence of RAB27a silencing, treatment with 250 nM A23187 for 5 min induced both the 'torn bag' pathway (Figure 5L) and MVE exocytosis (Figure 5K).

ATG5 silencing profoundly altered intracellular vesicular trafficking: the autophagosome formation was abolished (Figure 5O), while MVE abundance increased (Figure 5P) and exocytosis

became the dominant release route (Figure 5Q). Notably, the 'torn bag mechanism' was completely absent in ATG5-deficient cells and could not be induced by chloroquine treatment (Figure 5U-W), which otherwise strongly promoted both autophagosome accumulation (Figure 5R) and the 'torn bag' pathway when applied alone (Figure 5S,T). ATG5 silencing in HEK cells was not fully uniform. We were able to identify cells by TEM containing autophagosomes; however, these autophagosome-containing cells did not show accumulation of MVEs and no sign of MVE exocytosis was observed in these unsilenced cells.

The efficiency of gene silencing and its impact on autophagy were validated by confocal microscopy using HEK293T-PalmGFP-LC3RFP cells, which confirmed a significant reduction in the number of LC3-positive intracellular particles in the cytoplasm upon ATG5 knockdown (Figure 5X), while the size distribution of LC3-positive structures remained unchanged (Figure 5Y). These findings were further supported by RT-qPCR and Western blot analyses (Figure 5Z-AB), which demonstrated downregulation of ATG5 and RAB27a at both transcript and protein levels.

4 | Discussion

Recent studies revealed that EV biogenesis is considerably more complex than previously expected (Buzas 2023). In our earlier work, we identified MV-lEVs across multiple cell lines and in murine kidney and liver, originating from amphisomes and released as amphiectosomes. The limiting membrane of these structures spontaneously ruptures and discharges intraluminal vesicles into the extracellular space via the 'torn bag mechanism', a process that likely integrates endosomal and autophagic membrane systems. Notably, under homeostatic conditions, we found no ultrastructural evidence for the conventional sEV release through MVE exocytosis (Visnovitz et al. 2025). The present study aimed to better understand why MVE-derived exocytosis was not observed in our previous TEM analyses and to gain further insights into the mechanisms and regulatory pathways underlying both the amphiectosome-mediated 'torn bag mechanism' and MVE-driven exocytosis.

Our findings using HEK cells suggest that sEV secretion can be controlled by at least two distinct pathways: the autophagy-dependent amphiectosome release via the 'torn bag mechanism' and the classical exocytosis-dependent secretion of MVEs (Kowal et al. 2014; Dixson et al. 2023) and amphisomes (Jeppesen et al. 2019). These pathways may be differentially activated depending on cellular functional states.

In agreement with our previous findings (Visnovitz et al. 2025) under steady-state conditions, TEM consistently showed the 'torn bag mechanism'-mediated sEV release across all tested cell lines (Visnovitz et al. 2025) and mouse tissues (Figure 1A-O), whereas MVE exocytosis was undetectable. MV-lEV secretion and the 'torn bag mechanism' were unexpectedly frequent in mouse kidney and liver (Figure 1P) and may represent a 'default' steady-state sEV secretion route in non-stressed cells. Surprisingly, serum starvation induced MVE exocytosis in parallel with MV-lEV release and 'torn bag' sEV secretion (Figure 5C-F). This observation may be critical, as conventional EV studies and isolation protocols often rely on serum-free media (Théry et al. 2018), stress-inducing conditions (Koncz et al. 2023; Gebremedhn et al. 2020) or artificial stimulation of EV secretion (Williams et al. 2023; Aubertin et al. 2016; Ingato et al. 2018) all of which can alter the cellular origin and molecular composition of EVs.

Here, we took advantage of the HEK model system, which allows the straight forward generation of stable cell lines expressing multiple fluorescent proteins and enables efficient gene silencing by siRNA. In addition, since calcium influx is known to facilitate sEV secretion (Williams et al. 2023), Ca^{2+} ionophore treatment (A23187) was employed to discriminate between the relative contributions of the 'torn bag mechanism' and MVE exocytosis to sEV release.

It has been proposed that during calcium ionophore-induced sEV secretion, Ca^{2+} influx promotes membrane repair and vesicle fusion through ANX6-dependent mechanisms (Williams et al. 2023). Our data support this concept, as we observed a rapid induction of MVE exocytosis following A23187 treatment (Figure 2N,P-S,U-X). However, TEM analyses did not support an exclusive MVB origin of the released particles. Instead, the extracellular compartment contained a heterogeneous population of EV-like and non-EV structures, including likely lysosome-derived particles and damaged mitochondria (Figure 4A-I,L,M). These ultrastructural findings were further supported

FIGURE 4 | Analysis of the secretion of HEK293 cells induced by Ca^{2+} ionophore-mediated stress. TEM images of secreted particles under control conditions (A–C), 250 nM A23187 (D–F) and 500 nM A23187 (G–I) treatments. The majority of extracellular vesicles (EVs) are small EVs (<200 nm; indicated by white arrowheads) in the control condition, whereas a limited number of electron-dense lysosome-derived particles (black arrowheads) and a few damaged mitochondrion-derived structures (mt) are observed. With increasing the A23187 concentration, the abundance of lysosome-derived particles and damaged mitochondrion-derived particles increased (D–I). At 500 nM A23187 (G) a ruptured MV-lEV (tb) was detected. Quantitative analysis of EV diameters (J) demonstrates a concentration-dependent increase in vesicle size following A23187 treatments. Similarly, the proportion of lEVs (>200 nm) increases with elevated Ca^{2+}-ionophore concentration (K). The number of lysosome-derived (L) and mitochondrion-derived (M) particles exhibits a plateau-like increase with no significant difference between the 250 and 500 nM treatments, while both A23187 concentrations significantly elevate their abundance compared with control conditions. Proteomic analysis identified a total of 4713 proteins in the secretome (N) identified with at least two peptides. Most proteins were detected under both control and treated conditions; however, consistent with the TEM observations, 120 proteins were uniquely identified following Ca^{2+} ionophore treatments, the majority of which were present at both 250 and 500 nM concentrations. Based on quantitative proteomic analysis, a total of 81 proteins showed a global proteomic change between the sample groups. Principal component analysis (O) and heat map with hierarchical clustering (P) of these differentially expressed proteins revealed a complete separation of the groups. Panel (J) includes data from 390 to 623 EVs (from three independent ultrathin sections per condition), whereas panels (K–M) include averaged data from three to five independent ultrathin sections. Statistical significance was assessed using one-way ANOVA followed by Tukey's post hoc tests (*$p < 0.05$, **$p < 0.01$, ***$p < 0.001$, ****$p < 0.0001$). p values are available in Figure S4 statistics.xlsx.

TABLE 5 | GO classification of proteins uniquely detected in A23187-treated secretome samples and selected EV-associated markers.

Gene code	Protein name	Gene ontology result
Proteins present in 250 and 500 nM A23187 treatments but absent in control		
CTSL	Procathepsin L	Extracellular vesicles
PPP6R2	Serine/threonine-protein phosphatase 6 regulatory subunit 2	Autophagosome
FAS	Tumor necrosis factor receptor superfamily member 6	Plasma membrane
ABL2	Tyrosine-protein kinase ABL2	Plasma membrane
PXN	Paxillin	Plasma membrane
MPP2	MAGUK p55 subfamily member 2	Plasma membrane
ARHGEF6	Rho guanine nucleotide exchange factor 6	Plasma membrane
NAA35	N-alpha-acetyltransferase 35, NatC auxiliary subunit	Plasma membrane
CYP20A1	Cytochrome P450 20A1	Plasma membrane
SIRT2	NAD-dependent protein deacetylase sirtuin-2	Plasma membrane
EXOC6	Exocyst complex component 6	Plasma membrane
RAPGEF6	Rap guanine nucleotide exchange factor 6	Plasma membrane
SLC16A10	Monocarboxylate transporter 10	Plasma membrane
DTNBP1	Dysbindin	Plasma membrane
PANX1	Pannexin-1	Plasma membrane
MPHOSPH8	M-phase phosphoprotein 8	Plasma membrane
PIP5K1A	Phosphatidylinositol 4-phosphate 5-kinase type-1 alpha	Plasma membrane
TMEM120A	Ion channel TACAN	Plasma membrane
FAM234A	Protein FAM234A	Plasma membrane
PACC1	Proton-activated chloride channel	Plasma membrane
TM7SF3	Transmembrane 7 superfamily member 3	Plasma membrane
PLXNA1	Plexin-A1	Plasma membrane
ARL5B	ADP-ribosylation factor-like protein 5B	Lysosome
GALNS	N-acetylgalactosamine-6-sulfatase	Lysosome
ECE1	Endothelin-converting enzyme 1	Lysosome
CLN3	Battenin	Lysosome
MTM1	Myotubularin	Mitochondrial
BCKDHA	2-oxoisovalerate dehydrogenase subunit alpha, mitochondrial	Mitochondrial
ACADL	Long-chain specific acyl-CoA dehydrogenase, mitochondrial	Mitochondrial
MRPL28	Large ribosomal subunit protein bL28m	Mitochondrial
PDK1	[Pyruvate dehydrogenase (acetyl-transferring)] kinase isozyme 1, mitochondrial	Mitochondrial
TRMT5	tRNA (guanine(37)-N1)-methyltransferase	Mitochondrial
MTX3	Metaxin-3	Mitochondrial
ARMC10	Armadillo repeat-containing protein 10	Mitochondrial
OXR1	Oxidation resistance protein 1	Mitochondrial
MTERF3	Transcription termination factor 3, mitochondrial	Mitochondrial
ADO	2-aminoethanethiol dioxygenase	Mitochondrial
TIMM17A	Mitochondrial import inner membrane translocase subunit Tim17-A	Mitochondrial
NDUFAF1	Complex I intermediate-associated protein 30, mitochondrial	Mitochondrial
PFKFB2	6-phosphofructo-2-kinase/fructose-2,6-bisphosphatase 2	Mitochondrial
SYVN1	E3 ubiquitin-protein ligase synoviolin	Endosome
RDH10	Retinol dehydrogenase 10	Endosome

(Continues)

TABLE 5 | (Continued)

Gene code	Protein name	Gene ontology result
RFT1	Protein RFT1 homolog	Endosome
REEP4	Receptor expression-enhancing protein 4	Endosome
LRCH1	Leucine-rich repeat and calponin homology domain-containing protein 1	Endoplasmic reticulum
PRKAB1	5′-AMP-activated protein kinase subunit beta-1	Endoplasmic reticulum
NME7	Nucleoside diphosphate kinase 7	Endoplasmic reticulum
CAPN7	Calpain-7	Endoplasmic reticulum
OSBPL6	Oxysterol-binding protein-related protein 6	Endoplasmic reticulum
VIPAS39	Spermatogenesis-defective protein 39 homolog	Endoplasmic reticulum
TNIK	TRAF2 and NCK-interacting protein kinase	Endoplasmic reticulum
TAP2	Antigen peptide transporter 2	Endoplasmic reticulum
ALG11	GDP-Man:Man(3)GlcNAc(2)-PP-Dol alpha-1,2-mannosyltransferase	Endoplasmic reticulum
EXT2	Exostosin-2	Golgi apparatus
FKRP	Ribitol 5-phosphate transferase FKRP	Golgi apparatus
IFT172	Intraflagellar transport protein 172 homolog	Golgi apparatus
TRAPPC5	Trafficking protein particle complex subunit 5	Golgi apparatus
MINK1	Misshapen-like kinase 1	Golgi apparatus
UXS1	UDP-glucuronic acid decarboxylase 1	Golgi apparatus
GCAT	2-amino-3-ketobutyrate coenzyme A ligase, mitochondrial	Cytoplasm
DFFB	DNA fragmentation factor subunit beta	Cytoplasm
PHF14	PHD finger protein 14	Cytoplasm
RB1	Retinoblastoma-associated protein	Cytoplasm
PPP2R1B	Serine/threonine-protein phosphatase 2A 65 kDa regulatory subunit A beta isoform	Cytoplasm
CAMSAP2	Calmodulin-regulated spectrin-associated protein 2	Cytoplasm
TRIP11	Thyroid receptor-interacting protein 11	Cytoplasm
MYH14	Myosin-14	Cytoplasm
BRAP	BRCA1-associated protein	Cytoplasm
PTAR1	Protein prenyltransferase alpha subunit repeat-containing protein 1	Cytoplasm
IQGAP3	Ras GTPase-activating-like protein IQGAP3	Cytoplasm
WIPF2	WAS/WASL-interacting protein family member 2	Cytoplasm
CAMKK2	Calcium/calmodulin-dependent protein kinase kinase 2	Cytoplasm
MAP7D2	MAP7 domain-containing protein 2	Cytoplasm
REPIN1	Replication initiator 1	Cytoplasm
SMG9	Nonsense-mediated mRNA decay factor SMG9	Cytoplasm
AAMDC	Mth938 domain-containing protein	Cytoplasm
OTULINL	Inactive ubiquitin thioesterase OTULINL	Cytoplasm
CAMSAP3	Calmodulin-regulated spectrin-associated protein 3	Cytoplasm
SIN3B	Paired amphipathic helix protein Sin3b	Nucleus
ZNF324	Zinc finger protein 324A	Nucleus
YEATS4	YEATS domain-containing protein 4	Nucleus
WIZ	Protein Wiz	Nucleus
ELF1	ETS-related transcription factor Elf-1	Nucleus
PIP4K2B	Phosphatidylinositol 5-phosphate 4-kinase type-2 beta	Nucleus
CTDSPL2	CTD small phosphatase-like protein 2	Nucleus

(Continues)

TABLE 5 | (Continued)

Gene code	Protein name	Gene ontology result
EDRF1	Erythroid differentiation-related factor 1	Nucleus
SUGP1	SURP and G-patch domain-containing protein 1	Nucleus
CNEP1R1	Nuclear envelope phosphatase-regulatory subunit 1	Nucleus
KAT6A	Histone acetyltransferase KAT6A	Nucleus
NUDT16	U8 snoRNA-decapping enzyme	Nucleus
RBM33	RNA-binding protein 33	Nucleus
SMARCD1	SWI/SNF-related matrix-associated actin-dependent regulator of chromatin subfamily D member 1	Nucleus
ZNF512B	Zinc finger protein 512B	Nucleus
PNKP	Bifunctional polynucleotide phosphatase/kinase	Nucleus
FAM118B	Protein FAM118B	Nucleus
DIDO1	Death-inducer obliterator 1	Nucleus
DSCC1	Sister chromatid cohesion protein DCC1	Nucleus
UACA	Uveal autoantigen with coiled-coil domains and ankyrin repeats	Nucleus
BCAS3	BCAS3 microtubule associated cell migration factor	Nucleus
DCP1A	mRNA-decapping enzyme 1A	Nucleus
TASOR	Protein TASOR	Nucleus
PHF8	Histone lysine demethylase PHF8	Nucleus
MED16	Mediator of RNA polymerase II transcription subunit 16	Nucleus
GSDME	Gasdermin-E	Nucleus
ATP2B4	Plasma membrane calcium-transporting ATPase 4	Nucleus
Typical exosome, autophagosome and lysosomal markers in control and treated secretome		
CD9	CD9 antigen	Extracellular vesicle
TSG101	Tumor susceptibility gene 101 protein	Extracellular vesicle
CD63	CD63 antigen	Extracellular vesicle
CD81	CD81 antigen	Extracellular vesicle
LC3B	Microtubule-associated proteins 1A/1B light chain 3 beta 2	Autophagosome
LAMP1	Lysosome-associated membrane glycoprotein 1	Lysosome
LAMP2	Lysosome-associated membrane glycoprotein 2	Lysosome

by mass spectrometry-based secretomics, which revealed treatment-specific changes in the secreted protein repertoire, including the appearance of lysosomal and mitochondrial proteins (Table 5).

Our TEM observations suggest that under Ca^{2+} ionophore-induced stress, a broad range of membrane-enclosed intracellular compartments may be released, potentially contributing to membrane protection or stress adaptation. Notably, we did not observe the classical MVB exocytosis morphology previously described in the transferrin cycle of sheep reticulocytes (Pan et al. 1985). The transition from the 'torn bag mechanism' toward exocytosis-based sEV and particle secretion was accompanied by a concentration- and time-dependent increase in extracellular particle (EP) release, as quantified by nanoparticle tracking analysis (Figure 2AB-AD) and high-resolution flow cytometry (Figure 2AE). Furthermore, the discrepancy between scatter-based detection (Figure 2AB, AC) and lipid membrane dye labelling (Figure 2AD, AE) suggests that a substantial fraction of released EPs may lack a phospholipid membrane, indicating that not only MVBs but also other MVEs, such as lysosomes (Reddy et al. 2001), autophagosomes (Pallet et al. 2013) and amphisomes (Jeppesen et al. 2019) may contribute to the exocytotic process.

To clarify the molecular requirements of the 'torn bag mechanism' and MVE exocytosis, we modulated autophagy- and exocytosis-related pathways. ATG5 knockdown abolished amphiectosome formation, consistent with the impaired classical autophagy (Klionsky et al. 2021) and concomitantly suppressed the 'torn bag mechanism' (Figure 5O–Q,U–W), while promoting cytoplasmic MVE accumulation and exocytosis (Figure 5P,Q). This accumulation likely reflects a compensatory response to impaired amphiectosome release. Notably, not all cells exhibited the silenced phenotype based on TEM analysis. In silenced cells, the absence of autophagosomes was accompanied by MVE accu-

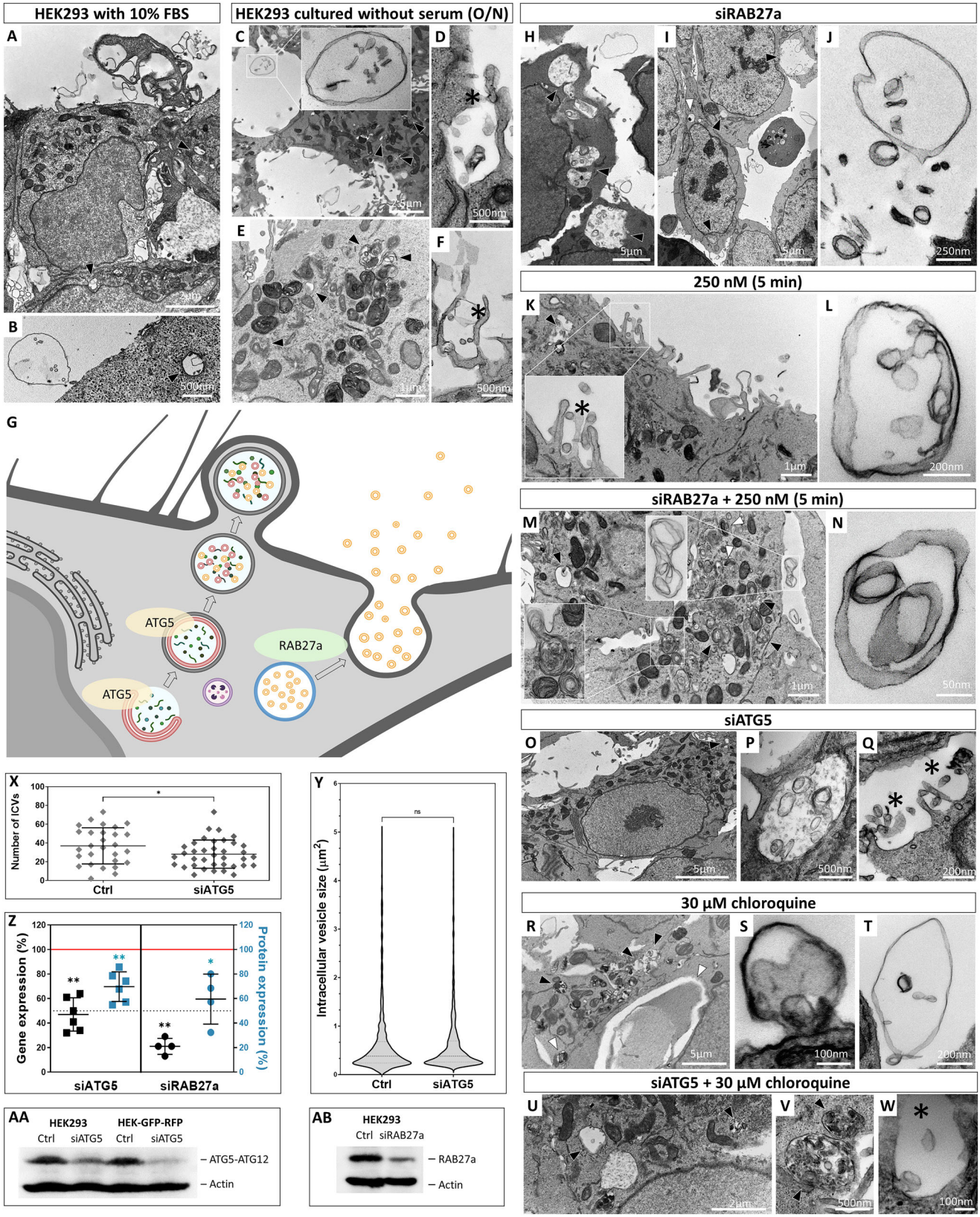

FIGURE 5 | Legend on next page.

mulation. In contrast, non- or partially silenced cells contained autophagosomes but showed no MVE cytoplasmic enrichment. In these cells, where autophagy was not properly inhibited, the predominant EV release remained MV-lEV secretion, without any detectable signs of MVE exocytosis.

These findings indicated that ATG5-dependent autophagy is required for amphiectosome biogenesis but is dispensable for MVE exocytosis. Conversely, RAB27a silencing, as expected (Ostrowski et al. 2010; Bobrie et al. 2012), selectively inhibited MVE exocytosis without affecting MV-lEV release or the 'torn bag mechanism', even under Ca^{2+} ionophore stimulation (Figure 5H-N).

Based on these results, we propose a two-pathway model of sEV secretion (Figure 6), in which amphiectosome release via the 'torn bag mechanism' represents a constitutive, autophagy-dependent pathway operating under steady state conditions. In contrast, MVE exocytosis constitutes a distinct pathway that is preferentially activated by stress. The differential involvement of RAB27a further underscores that these pathways are governed by distinct molecular machineries. Importantly, when autophagy is pharmacologically or genetically inhibited, amphiectosome formation and release are abolished, resulting in a compensatory shift toward sEV secretion via MVE exocytosis. Amphiectosome-mediated release may therefore maintain steady state sEV output, whereas MVE exocytosis serves as an inducible stress-responsive mechanism.

Immunocytochemical detection of plasma membrane-, CD63-, and LC3B-positive EPs (Figure 3A-G), together with live-cell imaging (Figure 3H-L), further supports this model. Saturation of EP release likely reflects the limited availability of amphiectosomes/MV-lEVs and MVEs. In live-cell imaging experiments, the transient increase in CD63 fluorescence observed at the 5-min time point following 250 and 500 nM A23187 treatment (Figure 3J,K) may indicate the recruitment of CD63-positive MVBs toward the plasma membrane. In parallel, the increased secretion of LC3-positive EPs (Figure 3G) together with the reduced intracellular LC3 fluorescence, is consistent with exocytosis of intracellular amphisomes. It should be emphasised that no unique marker exists for MVB-derived sEVs (Welsh et al. 2024; Mathieu et al. 2021). In agreement with our previous work (Visnovitz et al. 2025), we defined amphiectosomes as MV-lEVs containing either CD63- or LC3-positive intraluminal vesicles. While we assume that most LC3-positive sEVs originate from amphiectosomes, exocytosis of amphisomes (Jeppesen et al. 2019) cannot be excluded, particularly at the early 5 min time point following 250 nM A23187 treatment (Figure 3G,J), when this process may significantly contribute to LC3-positive EV release.

In summary, the data presented here challenge the prevailing assumption that MVE exocytosis represents the dominant route of sEV secretion under physiological conditions (Pan et al. 1985; Buschow et al. 2009; Deatherage and Cookson 2012; Escola et al. 1998; Raposo et al. 1996; Willms et al. 2016). Instead, we propose that amphiectosome/MV-lEV-mediated release constitutes the primary sEV secretion pathway in cellular homeostasis, whereas MVE exocytosis functions predominantly as a stress-responsive mechanism.

The discovery of MV-lEVs and amphiectosomes was only possible through investigations under steady state conditions using in situ fixation. Studying MV-lEVs and amphiectosomes is challenging due to their fragile limiting membrane. Mechanical stress during pipetting or centrifugation can rupture these membranes, leaving sEVs as the predominant population in most preparations (Visnovitz et al. 2025). In addition, during serum free culturing or when applying other stress-inducing conditions, MV-lEV secretion may be replaced by MVE exocytosis. Consequently, MV-lEV secretion and sEV release via the 'torn bag mechanism' can easily be overlooked. Based on the data presented here, the previously reported 'en bloc-released MVB-like EV clusters' (Valcz et al. 2019) can be identified as amphiectosomes. It remains to be established how the previously described large EVs containing ENPL (Koncz et al. 2023) or GFP-positive large EVs secreted following nanoinjection of cells by EV-like vesicles (Kovács et al. 2023) compare to amphiectosomes.

The paradigm shift from the exocytosis-only model to the alternative 'torn bag' or exocytosis two-pathway model may have significant implications for interpreting EV-based biomarkers

FIGURE 5 | Modulation of the two distinct sEV release pathways. Serum starvation and ATG5 or RAB27a silencing were performed. Ultrastructural changes were analysed by transmission electron microscopy (A–F, H–W), while silencing efficiency was assessed by confocal microscopy in HEK293T-PalmGFP-LC3RFP cells (X, Y), RT-qPCR (Z) and Western blot analysis (Z-AB). Under control conditions (A, B), the predominant sEV release mechanism was the 'torn bag' pathway. In the extracellular space, intact MV-lEVs (B) and empty membrane balloons (A) were observed. Serum starvation (C–F) induced MVE exocytosis (D, F) parallel to the 'torn bag mechanism' (C). MVEs accumulated in the cytoplasm (C, E) during serum starvation. The gene silencing strategy is summarised in Panel G https://BioRender.com/lsvxwwv. ATG5 regulates phagophore membrane formation, whereas RAB27a is a key protein in exocytosis-based sEV secretion. Modulating the expression of these proteins enabled us to influence the two main sEV release pathways: 'torn bag mechanism' and exocytosis. When RAB27a was silenced, sEV secretion occurred predominantly via the 'torn bag mechanism' (H–J) while MVE exocytosis was not detected, even under 250 nM A23187 treatment (M, N). In contrast, without RAB27a silencing, we observed both the 'torn bag mechanism' and the MVE exocytosis during 250 nM A23187 treatment (K, L). Silencing ATG5 abolished autophagosome formation (O), increased the abundance of MVE (P) and induced MVE exocytosis (Q). The 'torn bag mechanism' was absent and could not be reactivated even by chloroquine treatment (U–W). When chloroquine was applied alone, autophagosome formation and the 'torn bag mechanism' were both activated (R–T). MVEs are indicated by black arrowheads, autophagosome by white arrowheads, and MVE exocytosis by black asterisks. The effect of ATG5 silencing on autophagosome formation was confirmed by confocal microscopy using HEK293T-PalmGFP-LC3RFP cells (X, Y and Figure S5). Statistical significance was assessed by Student's *t* test on 27–36 cells (X), 994–1006 intracellular vesicles (ICV) (*$p < 0.05$, **$p < 0.01$). In the case of a gene expression study, the figure shows gene expression changes by ΔΔCt method, while statistical changes were calculated between ΔCt values. *p* values are available in Figure S5 statistics.xlsx.

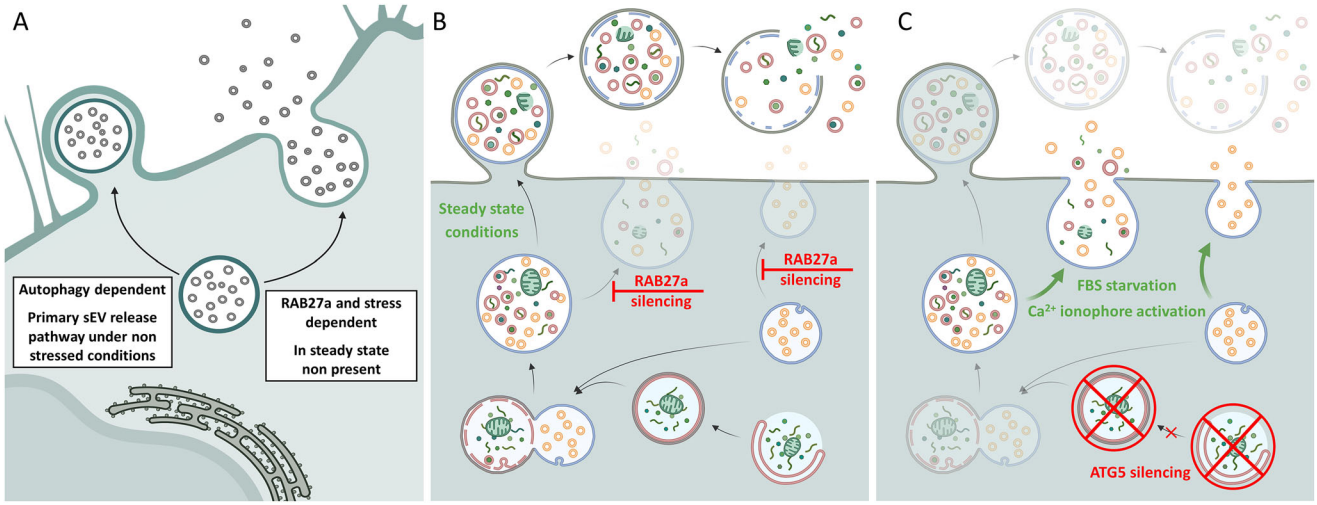

FIGURE 6 | Summary of the two sEV release mechanisms. Amphiectosome release with the 'torn bag mechanism' and MVE exocytosis represent two distinct sEV secretion pathways. The first pathway is autophagy-dependent and is the general and constitutive route under steady-state conditions. The second pathway appears to be more specific and is particularly activated under various stress conditions https://BioRender.com/d30dg27 (A). RAB27a does not appear to affect either amphisome release or 'torn bag'-mediated sEV secretion, but it inhibits MVE exocytosis https://BioRender.com/kfu5lxg (B). When autophagy is inhibited, amphiectosome release is blocked, and sEVs are secreted exclusively through exocytosis of MVE https://BioRender.com/042c4a2 (C).

and for designing therapeutic strategies that aim to modulate EV secretion.

Future work should address the functional consequences of these distinct EV populations, including their cargo composition and roles in intercellular communication under steady state and stress conditions. Additionally, elucidating the signalling pathways that govern the switch between these mechanisms will be critical for understanding EV biology in health and disease.

Author Contributions

Dorina Lenzinger: conceptualization, investigation, writing – original draft, writing – review and editing, methodology, validation, visualization, software, formal analysis, project administration, data curation. **Lilla Lankovics**: investigation, writing – review and editing. **István Dudás**: investigation, writing – review and editing. **Tünde Bárkai**: investigation, methodology. **Zsófia Szász**: investigation, writing – original draft, writing – review and editing, visualization, data curation. **Mirjam Balbisi**: investigation, writing – review and editing, writing – original draft, formal analysis, software, methodology, visualization, data curation. **Anthony Yan-Tang Wu**: investigation, writing – review and editing, writing – original draft, resources, data curation. **Krisztina V. Vukman**: investigation, funding acquisition, conceptualization, writing – original draft, writing – review and editing, methodology, formal analysis, supervision, resources. **Kelsey Fletcher**: investigation, methodology, writing – review and editing. **Attila Csomos**: investigation, writing – review and editing, data curation. **Zoltán Mucsi**: resources, supervision, writing – review and editing. **Edina Bugyik**: investigation, writing – review and editing. **Csaba Cserép**: investigation, methodology, visualization, writing – review and editing, resources. **Ádám Dénes**: resources, supervision, funding acquisition. **Szilvia Bősze**: investigation, funding acquisition, resources. **Lilla Turiák**: supervision, funding acquisition, software, formal analysis, data curation, resources, methodology. **Charles Pin-Kuang Lai**: funding acquisition, resources, supervision, validation. **Edit I. Buzás**: conceptualization, funding acquisition, writing – original draft, writing – review and editing, project administration, supervision, resources, methodology, validation, visualization, data curation. **Tamás Visnovitz**: conceptualization, investigation, funding acquisition, writing – original draft, methodology, visualization, writing – review and editing, formal analysis, supervision, resources, project administration, data curation, validation, software.

Acknowledgements

The authors gratefully acknowledge Anikó Gál and Györgyné Vidra for their valuable advice, as well as Soma Godó and Unicam Ltd. for making it possible to use the FluoView FV4000 confocal microscopy system. Éva Giessler, CEO of Bioxol Ltd., made the BioxML dye family available to us. Proteomic samples were run at the Institute of Science and Technology Austria LSF Mass Spectrometry Facility, part of the Scientific Service Units of the Institute of Science and Technology Austria. We acknowledge the Light Microscopy Centre at the Institute of Experimental Medicine for use of equipment (Abberior Instruments Facility Line STED microscope system).

Funding

This research was supported by the Hungarian National Research, Development and Innovation Office (NKFIH) through ADVANCED_25 grant (152112) which was awarded to T.V. and provided financial support for most of the experimental work presented in this study. The project was also supported by NVKP_16-1-2016-0004 and VEKOP-2.3.3-15-2017-00016, as well as by the Higher Education Excellence Program (FIKP) and the Therapeutic Thematic Programme (TKP2021-EGA-23). Additional support was provided by grants RRF-2.3.1-21-2022-00003 (National Cardiovascular Laboratory Program). The flow cytometry parts of the project were financed by the STARTING_25 grant (no. 152115), which was awarded to K.V.V. Some reagents were purchased from the NKFIH ADVANCED_grant (150767). The János Bolyai Research Scholarship of the Hungarian Academy of Sciences supported T.V. and C.C. Á.D. was funded by the 'Momentum' research grant from the Hungarian Academy of Sciences (grant number LP2022-5/2022) and the Hungarian Brain Research Program (grant number NAP2022-I-1/2022). A.C. was supported by the EKÖP-25 program by NKFIH. The secretome analysis was covered by the grant of L.T., who was supported by the Lendület (Momentum) Program of the Hungarian Academy of Sciences (grant number LP2023-19/2023). A.Y.-T.W. was supported by the Academia Sinica Postdoctoral

Scholar Program and the IAMS Junior Postdoctoral Fellowship. C.P.-K.L. was supported by the National Science and Technology Council (NSTC) under grant nos. NSTC 111-2628-B-001-022 and NSTC 114-2628-B-001-011, the Academia Sinica Innovative Materials and Analysis Technology Exploration (iMATE) Program Grant Number AS-iMATE-113-34 (C.P.-K.L.), the Academia Sinica Career Development Award No. AS-CDA-109-M04 (C.P.-K.L.).

Conflicts of Interest

E.I.B. is member of the Scientific Advisor Board of the Ludwig Boltzmann Institute for Nanovesicular Precision Medicine, Austria. T.V. is a scientific advisor of Bioxol Ltd. (Hungary). A.C. and Z.M. are employees of Brain Vision Center Research Institute and Competence Centre Ltd. (Hungary) and participated in the development of the BioxML dye family for Bioxol Ltd. (Hungary).

Data Availability Statement

Data available on request from the authors. Proteomics data are available in the MassIVE repository under the https://doi.org/10.25345/C5XW48954 link and can be downloaded via FTP (ftp://massive-ftp.ucsd.edu/v12/MSV000101713/).

References

Aubertin, K., A. K. A. Silva, N. Luciani, et al. 2016. "Massive Release of Extracellular Vesicles From Cancer Cells After Photodynamic Treatment or Chemotherapy." *Scientific Reports* 6: 35376. https://doi.org/10.1038/srep35376.

Benke, M., A. Zeöld, Á. Kittel, et al. 2023. "MiR-200b Categorizes Patients Into Pancreas Cystic Lesion Subgroups With Different Malignant Potential." *Scientific Reports* 13, no. 1: 19820. https://doi.org/10.1038/s41598-023-47129-1.

Bobrie, A., M. Colombo, S. Krumeich, G. Raposo, and C. Théry. 2012. "Diverse Subpopulations of Vesicles Secreted by Different Intracellular Mechanisms Are Present in Exosome Preparations Obtained by Differential Ultracentrifugation." *Journal of Extracellular Vesicles* 1: 18397. https://doi.org/10.3402/jev.v1i0.18397.

Buschow, S. I., E. N. M. Nolte-'t Hoen, G. Van Niel, et al. 2009. "MHC II in Dendritic Cells Is Targeted to Lysosomes or T Cell-Induced Exosomes via Distinct Multivesicular Body Pathways." *Traffic* 10, no. 10: 1528–1542. https://doi.org/10.1111/j.1600-0854.2009.00963.x.

Buzas, E. I. 2023. "The Roles of Extracellular Vesicles in the Immune System." *Nature Reviews Immunology* 23, no. 4: 236–250. https://doi.org/10.1038/s41577-022-00763-8.

Campeau, E., V. E. Ruhl, F. Rodier, et al. 2009. "A Versatile Viral System for Expression and Depletion of Proteins in Mammalian Cells." *PLoS ONE* 4, no. 8: e6529. https://doi.org/10.1371/journal.pone.0006529.

Deatherage, B. L., and B. T. Cookson. 2012. "Membrane Vesicle Release in Bacteria, Eukaryotes, and Archaea: A Conserved yet Underappreciated Aspect of Microbial Life." *Infection and Immunity* 80, no. 6: 1948–1957. https://doi.org/10.1128/IAI.06014-11.

Demichev, V., C. B. Messner, S. I. Vernardis, K. S. Lilley, and M. Ralser. 2020. "DIA-NN: Neural Networks and Interference Correction Enable Deep Proteome Coverage in High Throughput." *Nature Methods* 17, no. 1: 41–44. https://doi.org/10.1038/s41592-019-0638-x.

De Paoli, S. H., T. Z. Tegegn, O. K. Elhelu, et al. 2018. "Dissecting the Biochemical Architecture and Morphological Release Pathways of the Human Platelet Extracellular Vesiculome." *Cellular and Molecular Life Sciences* 75, no. 20: 3781–3801.

Dixson, A. C., T. R. Dawson, D. Di Vizio, and A. M. Weaver. 2023. "Context-Specific Regulation of Extracellular Vesicle Biogenesis and Cargo Selection." *Nature Reviews Molecular Cell Biology* 24, no. 7: 454–476. https://doi.org/10.1038/s41580-023-00576-0.

Escola, J.-M., M. J. Kleijmeer, W. Stoorvogel, J. M. Griffith, O. Yoshie, and H. J. Geuze. 1998. "Selective Enrichment of Tetraspan Proteins on the Internal Vesicles of Multivesicular Endosomes and on Exosomes Secreted by Human B-lymphocytes." *Journal of Biological Chemistry* 273, no. 32: 20121–20127. https://doi.org/10.1074/jbc.273.32.20121.

Gebremedhn, S., A. Gad, H. S. Aglan, et al. 2020. "Extracellular Vesicles Shuttle Protective Messages Against Heat Stress in Bovine Granulosa Cells." *Scientific Reports* 10, no. 1: 15824. https://doi.org/10.1038/s41598-020-72706-z.

Harding, C., J. Heuser, and P. Stahl. 1983. "Receptor-Mediated Endocytosis of Transferrin and Recycling of the Transferrin Receptor in Rat Reticulocytes." *Journal of cell biology* 97, no. 2: 329–339. https://doi.org/10.1083/jcb.97.2.329.

Ingato, D., J. A. Edson, M. Zakharian, and Y. J. Kwon. 2018. "Cancer Cell-Derived, Drug-Loaded Nanovesicles Induced by Sulfhydryl-Blocking for Effective and Safe Cancer Therapy." *ACS Nano* 12, no. 9: 9568–9577. https://doi.org/10.1021/acsnano.8b05377.

Jeppesen, D. K., A. M. Fenix, J. L. Franklin, et al. 2019. "Reassessment of Exosome Composition." *Cell* 177, no. 2: 428–445.e18. https://doi.org/10.1016/j.cell.2019.02.029.

Kawano, F., H. Suzuki, A. Furuya, and M. Sato. 2015. "Engineered Pairs of Distinct Photoswitches for Optogenetic Control of Cellular Proteins." *Nature Communications* 6: 6256. https://doi.org/10.1038/ncomms7256.

Klionsky, D. J., A. K. Abdel-Aziz, S. Abdelfatah, et al. 2021. "Guidelines for the Use and Interpretation of Assays for Monitoring Autophagy (4th Edition)[1]." *Autophagy* 17, no. 1: 1–382. https://doi.org/10.1080/15548627.2020.1797280.

Koncz, A., L. Turiák, K. Németh, et al. 2023. "Endoplasmin Is a Hypoxia-Inducible Endoplasmic Reticulum-Derived Cargo of Extracellular Vesicles Released by Cardiac Cell Lines." *Membranes* 13: 431. https://doi.org/10.3390/membranes13040431.

Koontz, L. 2014. "TCA Precipitation." *Methods in Enzymology* 541: 3–10. https://doi.org/10.1016/B978-0-12-420119-4.00001-X.

Kovács, K. D., T. Visnovitz, T. Gerecsei, et al. 2023. "Nanoinjection of Extracellular Vesicles to Single Live Cells by Robotic Fluidic Force Microscopy." *Journal of Extracellular Vesicles* 12, no. 12: 12388. https://doi.org/10.1002/jev2.12388.

Kowal, J., M. Tkach, and C. Théry. 2014. "Biogenesis and Secretion of Exosomes." *Current Opinion in Cell Biology* 29: 116–125. https://doi.org/10.1016/j.ceb.2014.05.004.

Kowarik, A., and M. Templ. 2016. "Imputation With the R Package VIM." *Journal of Statistical Software* 74, no. 7: 1–16. https://doi.org/10.18637/jss.v074.i07.

Lai, C. P., E. Y. Kim, C. E. Badr, et al. 2015. "Visualization and Tracking of Tumour Extracellular Vesicle Delivery and RNA Translation Using Multiplexed Reporters." *Nature Communications* 6, no. 1: 7029. https://doi.org/10.1038/ncomms8029.

Mathieu, M., N. Névo, M. Jouve, et al. 2021. "Specificities of Exosome Versus Small Ectosome Secretion Revealed by Live Intracellular Tracking of CD63 and CD9." *Nature Communications* 12, no. 1: 4389. https://doi.org/10.1038/s41467-021-24384-2.

Németh, K., Z. Varga, D. Lenzinger, et al. 2021. "Extracellular Vesicle Release and Uptake by the Liver Under Normo- and Hyperlipidemia." *Cellular and Molecular Life Sciences* 78, no. 23: 7589–7604.

Nishihara, R., R. Paulmurugan, T. Nakajima, et al. 2019. "Highly Bright and Stable NIR-BRET With Blue-Shifted Coelenterazine Derivatives for Deep-Tissue Imaging of Molecular Events In Vivo." *Theranostics* 9, no. 9: 2646–2661. https://doi.org/10.7150/thno.32219.

Olah, I., C. Kendall, and B. Glick. 1992. "Differentiation of Bursal Secretory-Dendritic Cells Studied With Anti-Vimentin Monoclonal Antibody." *Anatomical Record* 233, no. 1: 111–120. https://doi.org/10.1002/ar.1092330115.

Ostrowski, M., N. B. Carmo, S. Krumeich, et al. 2010. "Rab27a and Rab27b Control Different Steps of the Exosome Secretion Pathway." *Nature Cell Biology* 12, no. 1: 19–30. https://doi.org/10.1038/ncb2000.

Pallet, N., I. Sirois, C. Bell, et al. 2013. "A Comprehensive Characterization of Membrane Vesicles Released by Autophagic Human Endothelial Cells." *Proteomics* 13, no. 7: 1108–1120. https://doi.org/10.1002/pmic.201200531.

Pan, B. T., K. Teng, C. Wu, M. Adam, and R. M. Johnstone. 1985. "Electron Microscopic Evidence for Externalization of the Transferrin Receptor in Vesicular Form in Sheep Reticulocytes." *Journal of Cell Biology* 101, no. 3: 942–948. https://doi.org/10.1083/jcb.101.3.942.

Raposo, G., H. W. Nijman, W. Stoorvogel, et al. 1996. "B Lymphocytes Secrete Antigen-Presenting Vesicles." *Journal of Experimental Medicine* 183, no. 3: 1161–1172. https://doi.org/10.1084/jem.183.3.1161.

Raposo, G., and W. Stoorvogel. 2013. "Extracellular Vesicles: Exosomes, Microvesicles, and Friends." *Journal of Cell Biology* 200, no. 4: 373–383. https://doi.org/10.1083/jcb.201211138.

Reddy, A., E. V. Caler, and N. W. Andrews. 2001. "Plasma Membrane Repair Is Mediated by Ca2+-Regulated Exocytosis of Lysosomes." *Cell* 106, no. 2: 157–169. https://doi.org/10.1016/S0092-8674(01)00421-4.

Relucenti, M., F. Francescangeli, M. L. De Angelis, et al. 2022. "A Different Exosome Secretion Pattern Characterizes Patient-Derived Colorectal Cancer Multicellular Spheroids and Their Mouse Xenografts." *Biology* 11: 1427. https://doi.org/10.3390/biology11101427.

Reynolds, E. S. 1963. "The Use of Lead Citrate at High pH as an Electron-Opaque Stain in Electron Microscopy." *Journal of Cell Biology* 17, no. 1: 208–212. https://doi.org/10.1083/jcb.17.1.208.

Ritchie, M. E., B. Phipson, D. Wu, et al. 2015. "Limma Powers Differential Expression Analyses for RNA-Sequencing and Microarray Studies." *Nucleic Acids Research* 43, no. 7: e47–e47. https://doi.org/10.1093/nar/gkv007.

Saito, K., Y.-F. Chang, K. Horikawa, et al. 2012. "Luminescent Proteins for High-Speed Single-Cell and Whole-Body Imaging." *Nature Communications* 3: 1262. https://doi.org/10.1038/ncomms2248.

Skowronek, P., M. Thielert, E. Voytik, et al. 2022. "Rapid and In-Depth Coverage of the (Phospho-)Proteome With Deep Libraries and Optimal Window Design for Dia-PASEF." *Molecular & Cellular Proteomics* 21, no. 9: 100279. https://doi.org/10.1016/j.mcpro.2022.100279.

Szász, Z., K. N. Enyedi, A. Takács, et al. 2024. "Characterisation of the Cell and Molecular Biological Effect of Peptide-Based Daunorubicin Conjugates Developed for Targeting Pancreatic Adenocarcinoma (PANC-1) Cell Line." *Biomedicine & Pharmacotherapy* 173: 116293. https://doi.org/10.1016/j.biopha.2024.116293.

Szász, Z., A. Takács, M. Kalabay, et al. 2025. "Comparative Study of the Anti-Tumour Effects of the Imipridone, ONC201 and Its Fluorinated Analogues on Pancreatic Cancer Cell Line." *Scientific Reports* 15, no. 1: 15925. https://doi.org/10.1038/s41598-025-00070-x.

Théry, C., K. W. Witwer, E. Aikawa, et al. 2018. "Minimal Information for Studies of Extracellular Vesicles 2018 (MISEV2018): A Position Statement of the International Society for Extracellular Vesicles and Update of the MISEV2014 Guidelines." *Journal of Extracellular Vesicles* 7, no. 1: 1535750.

Valcz, G., E. I. Buzás, Á. Kittel, et al. 2019. "En Bloc Release of MVB-Like Small Extracellular Vesicle Clusters by Colorectal Carcinoma Cells." *Journal of Extracellular Vesicles* 8, no. 1: 1596668. https://doi.org/10.1080/20013078.2019.1596668.

van Niel, G., G. D'Angelo, and G. Raposo. 2018. "Shedding Light on the Cell Biology of Extracellular Vesicles." *Nature Reviews Molecular Cell Biology* 19, no. 4: 213–228.

Visnovitz, T., D. Lenzinger, A. Koncz, et al. 2025. "A 'Torn Bag Mechanism' of Small Extracellular Vesicle Release via Limiting Membrane Rupture of En Bloc Released Amphisomes (Amphiectosomes)." *Elife* 13: RP95828. https://doi.org/10.7554/eLife.95828.

Visnovitz, T., Á. Solti, G. Csikós, and W. Fricke. 2012. "Plasma Membrane H^+-ATPase Gene Expression, Protein Level and Activity in Growing and Non-Growing Regions of Barley (*Hordeum vulgare*) Leaves." *Physiologia Plantarum* 144, no. 4: 382–393. https://doi.org/10.1111/j.1399-3054.2012.01578.x.

Welsh, J. A., D. C. I. Goberdhan, L. O'Driscoll, et al. 2024. "Minimal Information for Studies of Extracellular Vesicles (MISEV2023): From Basic to Advanced Approaches." *Journal of Extracellular Vesicles* 13, no. 2: e12404. https://doi.org/10.1002/jev2.12404.

Williams, J. K., J. M. Ngo, I. M. Lehman, and R. Schekman. 2023. "Annexin A6 Mediates Calcium-Dependent Exosome Secretion During Plasma Membrane Repair." *Elife* 12: e86556. https://doi.org/10.7554/eLife.86556.

Willms, E., H. J. Johansson, I. Mäger, et al. 2016. "Cells Release Subpopulations of Exosomes With Distinct Molecular and Biological Properties." *Scientific Reports* 6: 22519. https://doi.org/10.1038/srep22519.

Wu, A. Y.-T., Y.-C. Sung, Y.-J. Chen, et al. 2020. "Multiresolution Imaging Using Bioluminescence Resonance Energy Transfer Identifies Distinct Biodistribution Profiles of Extracellular Vesicles and Exomeres With Redirected Tropism." *Advanced Science* 7, no. 19: 2001467. https://doi.org/10.1002/advs.202001467.

Supporting Information

Additional supporting information can be found online in the Supporting Information section.

Supplementary Figure: jev270345-sup-0001-Figure1.xlsx **Supplementary Figure**: jev270345-sup-0002-Figure2.xlsx **Supplementary Figure**: jev270345-sup-0003-Figure3.xlsx **Supplementary Figure**: jev270345-sup-0004-Figure4.xlsx **Supplementary Figure**: jev270345-sup-0005-Figure5.xlsx **Supplementary materials**: jev270345-sup-0006-SuppMat.xlsx **Supplementary materials**: jev270345-sup-0007-SuppMat.docx